

Post-Print of an Accepted Manuscript on the Laboratory of Turbulent Flows Website

Complete citation:

Rowin, W. A., & Ghaemi, S. (2019). Streamwise and spanwise slip over a superhydrophobic surface. *Journal of fluid mechanics*, 870, 1127-1157. doi: 10.1017/jfm.2019.225

The final publication is available at <https://doi.org/10.1017/jfm.2019.225>

The Cambridge University Press is the copyright holder; however, permission to post the Accepted Manuscript on the Laboratory's Website is retained under the transfer of copyright.

The Accepted Manuscript begins on the next page.

Streamwise and spanwise slip over a superhydrophobic surface

WAGIH ABU ROWIN AND SINA GHAEMI

Department of Mechanical Engineering, University of Alberta
Edmonton, Alberta T6G 2G8, Canada

The near-wall turbulent flow over a superhydrophobic surface (SHS) with random texture was studied using three-dimensional Lagrangian particle tracking velocimetry (3D-PTV). The channel was operated at a constant mass flow rate over the SHS and a smooth surface at a Reynolds number of 7000 based on the bulk velocity of 0.93 m/s and the full channel height. The friction Reynolds number was 217, based on the friction velocity and half channel height. The 3D-PTV processing was based on the shake-the-box algorithm applied to images of fluorescent tracers recorded using four high-speed cameras. The SHS was obtained by spray coating, resulting in a root-mean-square roughness of 0.29λ and the average texture width of 5.0λ , where $\lambda = 17 \mu\text{m}$ is the inner flow scale over the SHS. The 3D-PTV measurements confirmed an isotropic slip with a streamwise slip length of 5.9λ and a spanwise slip length of 5.9λ . As a result, both the near-wall mean streamwise and spanwise velocity profiles over the SHS were higher than the smooth surface. The streamwise and spanwise slip velocities over the SHS were 0.27 m/s and 0.018 m/s, respectively. The near-wall Reynolds stresses over the SHS were larger and shifted towards the wall when normalized by the corresponding inner scaling, despite the smaller friction Reynolds number of 180 over the SHS. The near-wall measurement of streamwise velocity showed that the shear-free pattern consists of streamwise elongated regions with a length of 800λ and a spanwise width of 300λ . The plastron dimensions correspond to the mean distance of the largest roughness peaks ($20 \mu\text{m}$) obtained from profilometry of the SHS. The drag reduction over the SHS was 30-38% as estimated from pressure measurement and the flow field using the 3D-PTV.

Key words: superhydrophobic, slip velocity, turbulent channel flow, three-dimensional particle tracking velocimetry

1. Introduction

Skin-friction forms a large portion of the drag forces in industrial applications that involve turbulent wall flows, such as pipelines and marine vehicles. Therefore flow control techniques that reduce skin friction are of interest and have been extensively investigated. A relatively recent technique for reduction of skin friction is based on introducing an air layer between the liquid flow and the solid surface to allow the liquid to *slip* over the solid surface (Rothstein 2010). This type of boundary condition can be applied using a superhydrophobic surface (SHS), which typically consist of a surface with micro/nano-scale pores covered with a water-repellent coating. When submerged in water, the pores of the SHS hold small air bubbles or a complete layer of air (i.e. a plastron). This interface prevents the surface from being in direct contact with water and results in water slipping over the air layer.

In laminar channel flows, several pioneering investigations by Ou *et al.* (2004), Ou & Rothstein (2005), Choi *et al.* (2006), and Joseph *et al.* (2006) have confirmed up to 60% drag reduction (DR). The DR was observed to directly depend on the slip velocity and is a function of the surface area covered by air. However, measurements in turbulent flows over SHSs have demonstrated scattered results: different values of DR and occasional drag increases. The DR variations are not only associated with the superhydrophobicity level of the surface, which can be best characterized by contact angle hysteresis (Gose *et al.* 2018). Several experiments have shown that the efficacy of the surfaces also depends on surface roughness (Aljallis *et al.* 2013; Ling *et al.* 2016), the level of dissolved air in water (Ling *et al.* 2017), wall shear stress (Vajdi Hokmabad & Ghaemi 2017), and hydrostatic pressure (Lei *et al.* 2009; Dilip *et al.* 2014; Gose *et al.* 2018). These parameters affect the morphology and thickness (Reholon & Ghaemi 2018) and the longevity of the air phase (Samaha *et al.* 2012), which subsequently affect the slip velocity. In addition, fluid slip can be in the streamwise and spanwise directions, which affects the wall shear stress in different ways.

The slip velocity over a surface is characterized in the form of Navier slip-boundary condition in both the streamwise (x) and spanwise (z) directions as

$$U_s = l_x \left. \frac{\partial \langle U \rangle}{\partial y} \right|_{y=0}, \quad W_s = l_z \left. \frac{\partial \langle W \rangle}{\partial y} \right|_{y=0}. \quad (1.1)$$

Here U and W are the velocity components and l_x and l_z are the effective slip lengths in the streamwise and spanwise directions, respectively. The wall-normal axis is indicated by y and the subscript s denotes slip velocity. The $\langle \rangle$ symbol refers to ensemble averaging of velocity in time and in the x and z -directions. As it is seen in this equation, slip velocity is linearly proportional to slip length.

The direct numerical simulation (DNS) of Min & Kim (2004) assumed a homogenous surface while imposed independent values of effective slip length in the streamwise and spanwise directions (i.e. $l_x \neq 0, l_z \neq 0$). Their investigation showed that an imposed l_x reduces the drag, while l_z results in a drag increase. However, DR due to l_x was larger than the increase of drag due to a similar value of l_z . They contributed the increase of drag by l_z to the intensification of the near-wall streamwise vortices. Fukagata *et al.* (2006) estimated the DR of a SHS using an analytical model based on l_x and l_z , also assuming a homogenous slip-boundary condition. They concluded that the mechanism of the decrease in drag by l_x and the increase in drag by l_z can be assumed independent of each other, based on the evaluation of their model using the DNS of Min & Kim (2004). Busse & Sandham (2012) mapped contours of drag versus l_x and l_z from a DNS of turbulent channel flow to study the effect of anisotropic boundary condition. They reported that the drag increase due to l_z reaches an asymptote of about 50% drag increase when l_z increases beyond 10λ (λ is the inner length-scale of the turbulent flow). However, for large l_x exceeding 10λ , DR is independent of l_z . Busse & Sandham (2012) also observed that a finite value of l_x makes the near-wall streaks more organized, while l_z disrupts the coherence of the streaks. These numerical simulations have shed light on the effect of slip anisotropy on DR.

In experimental investigations, the streamwise and spanwise slip lengths are coupled and depend on the morphology of the air phase over the SHS texture. However, a macroscopic surface anisotropy can be obtained using an organized surface pattern, which can result in different values of l_x and l_z . For example, Woolford *et al.* (2009) investigated two SHSs with $4 \mu\text{m}$ ribs and a cavity width of $32 \mu\text{m}$ oriented in both the streamwise and spanwise directions in a turbulent channel flow. The SHS with streamwise ribs reduced the drag while the SHS with spanwise ribs

increased the drag. Park *et al.* (2014) varied the area of the air-water interface over a SHS with streamwise micro-grates. They measured up to 75% DR when the air-water interface covered 95% of the surface. More recently, the experiment of Ling *et al.* (2016) reported that a SHS with streamwise grooves, manufactured by preferential polishing, results in a higher DR compared to a surface with a random isotropic pattern. These investigations demonstrated the effect of surface pattern and the morphology of the air-water interface on drag. Considering the numerical results of Min & Kim (2004) and Busse & Sandham (2012), it can be conjectured that the large DR cases are associated with a large l_x , while the drag increase cases are due to a large l_z . However, the experiments did not measure the spanwise slip and did not indicate if the surface induces an anisotropic slip or modulates turbulence through the slip-free pattern.

Instead of prescribing an effective slip length, the numerical simulation of Martell *et al.* (2009) modeled the SHS as a grid of slip-free and no-slip regions. They concluded that U_s and l_x increase by increasing the slip-free area. Park *et al.* (2013) also conducted simulations in laminar and turbulent channel flows over a SHS with streamwise ribs. Through comparison with the laminar flow, they associated the larger DR of the SHS in the turbulent regime with attenuation of turbulence structures. Rastegari & Akhavan (2015) decomposed the DR equation of Fukagata *et al.* (2002) into two terms; the first term shows the direct effect of slip velocity on drag, and the second term shows attenuation of turbulence. Their investigation showed that 80 to 100% of the DR over micro-pattered surfaces was due to the term describing the direct effect of slip velocity. Rastegari & Akhavan (2015) also investigated different surface patterns with streamwise spanwise and micro-post patterns using DNS. They obtained 20% DR using a SHS with spanwise grooves that have an 87.5% slip-free area. This observation suggest that the spanwise grooves generated a streamwise slip to result in the 20% DR. Although this may not be unexpected, it highlights the importance of investigating the relation between surface morphology and the strength of streamwise and spanwise slip (i.e. slip anisotropy).

The effect of a SHS on the mean velocity and turbulent statistics has been extensively investigated in the past. In the near-wall region, mean velocity increases because of the slip velocity (Daniello *et al.* 2009; Woolford *et al.* 2009; Ling *et al.* 2016; Abu Rowin *et al.* 2017). In channel flows, the mean velocity reduces away from the wall to maintain the same mass flow rate (Woolford *et al.* 2009; Abu Rowin *et al.* 2017). Only a few studies have measured the slip velocity over SHSs in the turbulent regime using measurement techniques with high spatial resolution. Ling *et al.* (2016) measured the slip velocity over SHSs with a wide range of roughnesses in a turbulent boundary layer using digital holographic microscopy (DHM). They reported $U_s = 0.73$ m/s (0.36 of the bulk velocity, U_b) over a SHS with 36% DR at a free-stream velocity of 2.0 m/s. Abu Rowin *et al.* (2017) reported a 0.023 m/s slip velocity at a bulk channel velocity of 0.173 m/s ($0.13U_b$) using long-range microscopic particle tracking velocimetry (PTV) over a SHS with 19% DR.

The effect of slip velocity on the Reynolds stresses has been typically evaluated by comparison with a surface with a no-slip boundary condition (i.e. smooth surface) under the same bulk flow conditions. If the Reynolds stresses are normalized with the friction velocity of the smooth surface a reduction in the streamwise wall-normal, and shear Reynolds stresses are observed in the outer layer as seen in the experiments of Woolford *et al.* (2009), Vajdi Hokmabad & Ghaemi (2016), and Ling *et al.* (2016). However, closer to the wall at $y < 10\lambda$, the streamwise Reynolds stress, $\langle u^2 \rangle$, and shear Reynolds stress, $\langle uv \rangle$, are larger than those over the smooth surface (Ling *et al.* 2016; Abu Rowin *et al.* 2017). The increase in $\langle u^2 \rangle$ is associated with the increase of fluctuations by relaxing the no-slip boundary condition. On the other hand, the increase in $\langle uv \rangle$ is mostly

associated with the roughness of the SHS as discussed by Abu Rowin *et al.* (2017). The near-wall wall-normal Reynolds stress, $\langle v^2 \rangle$, remains comparable to that over the smooth surface due to the non-permeable boundary condition for SHSs with low roughness (Abu Rowin *et al.* 2017). Ling *et al.* (2016) reported an increase of $\langle v^2 \rangle$ near the SHS, which is presumably due to the high roughness of their tested surfaces. The numerical studies have also confirmed these trends (Min & Kim 2004; Busse & Sandham 2012; Rastegari & Akhavan 2015), although the observed increase in near-wall Reynolds shear stress is negligible due to lack of roughness in these simulations. A near-wall increase of spanwise Reynolds stress, $\langle w^2 \rangle$, was also observed in the DNS of Min & Kim (2004) when a spanwise slip ($l_z \neq 0$) was imposed. Rastegari & Akhavan (2015) observed an increase of $\langle w^2 \rangle$ over SHSs with spanwise and streamwise microgrooves. The latter case suggests the presence of spanwise slip over streamwise microgrooves. The characterization of the effective slip length and its anisotropy is of particular importance for simulation of SHSs with random texture. However, there has been no experimental investigation of the magnitude of spanwise slip over a SHS in turbulent flows.

Most of the numerical studies over SHSs modeled the surface as an organized pattern of alternating regions of slip and no-slip boundary condition (e.g. Martell *et al.* 2009, 2010; Park *et al.* 2013; Türk *et al.* 2014; Lee *et al.* 2015; Seo *et al.* 2018). To the authors' knowledge there are two recent numerical investigations of turbulent flows over randomly patterned SHSs. The numerical simulation of Seo & Mani (2018) modeled the SHS as a random pattern of no-slip posts with identical height. They reported that the random distribution of the posts results in 30% smaller effective slip length due to interruption of the shear-free regions when compared with a surface with an organized pattern. Seo & Mani (2018) indicated that a homogeneous isotropic slip length ($l_x = l_z$) can be applied when the roughness elements are small ($\sim 4\lambda$), while this model fails for surfaces with larger roughness ($\sim 26\lambda$). The numerical study of Alame & Mahesh (2018) modeled the flow over a more realistic SHS with a random pattern obtained from profile measurement over a sandblasted aluminum substrate. They observed that the shear-free interface attenuates the turbulence intensities while the surface roughness increases turbulence.

Development of numerical simulations of turbulent flow over SHSs benefits from an experimental characterization of slip anisotropy ($l_x \neq l_z$) and its inhomogeneity over the SHS. This can be accomplished by measurement of streamwise and spanwise slip velocities in the linear viscous sublayer. Such a measurement can investigate if the isotropy assumption is accurate for modeling SHSs and if it is possible to vary the slip anisotropy of SHSs. Experiments can also investigate the homogeneity of the shear-free pattern over SHSs. Due to the surface roughness, variation in hydrostatic pressure, shear, and dissolved oxygen level, the plastron may not form a flat shear-free interface. Characterization of the plastron morphology and the consequent shear-free pattern is also important for SHS modeling to assist in the evaluation of numerical simulations, and to design SHSs. Such an experimental characterization of isotropy and homogeneity of slip velocity requires three-dimensional measurement of flow velocity with high-spatial resolution in the inner layer.

The present investigation measures slip velocity in both the streamwise and spanwise directions over a spray-coated SHS with a random texture. The investigation also characterizes the near-wall Reynolds stresses and the inhomogeneity of the shear-free interface. The experiment is conducted in a turbulent channel flow at $Re_\tau = 217$ (based on the friction velocity and the half channel height). The measurements are carried out using state-of-the-art three-dimensional-PTV (3D-PTV) based on the shake-the-box algorithm (Schanz *et al.* 2013, 2016). This method can provide accurate measurement of the near-wall velocity with high spatial-resolution (Schröder et

al. 2015; Novara *et al.* 2016). Pressure drop measurement over the SHS is also implemented to evaluate drag estimation from 3D-PTV.

2. Experimental apparatus and procedures

Details of the flow facility including the pressure drop measurements and the channel flow parameters are listed in this section. The preparation of the SHS is explained, followed by its characterization using scanning electron microscopy, contact angle measurement, and profilometer measurement. Finally, the time-resolved 3D-PTV for characterization of the inner layer of the turbulent channel flow is discussed here.

2.1 Turbulent channel flow facility

The experiments were conducted in a closed-circuit turbulent channel flow as shown in the schematic of figure 1. The test section had a rectangular cross-section with a height of $H = 6$ mm, width of $W = 40$ mm, and total length of 1.2 m ($200H$). The aspect ratio (W/H) of the channel cross-section was 6.7. This aspect ratio is close to the minimum recommended aspect ratio of 7 by Dean (1978) to maintain a 2D flow in the center of the channel. The investigation of Vinuesa *et al.* (2014) also showed negligible effect ($\sim 1\%$) on centerline Reynolds stresses for a channel with an aspect ratio of 7. The top and bottom walls of the channel were made of transparent acrylic while the side walls were made of glass. The coordinate system in the streamwise wall-normal, and spanwise directions is indicated with x , y , and z as displayed in figure 1. The settling chamber upstream of the test section had a diameter of 82.5 mm and includes a honeycomb structure to break down the large eddies. The chamber was connected to the test section through a three-dimensional contraction, which was manufactured by 3D-printing and coated with epoxy. The contraction ratio with respect to the diameter of the chamber was 14:1 in the y -direction and 2:1 in the z -direction. The loop was equipped with a centrifugal pump controlled by a variable frequency driver (VFD). An electromagnetic flow meter (FLR6305D, Omega Engineering, Inc., USA) was used to monitor the mass flow rate. A proportional-integral-derivative (PID) controller was developed with commercial software (LabView 2016, National Instruments) to control the flow rate. The PID controller communicated with the VFD to control the pump rpm through an input/output card (NI USB-6001, National Instruments).

The pressure difference (dP) over the test surface was monitored using a pressure transducer (P15, Validyne) with a 0.2 psi diaphragm. The transducer was connected to two pressure ports at the upstream and downstream of the test surface with a distance of 276 mm ($46H$). The uncertainty of the pressure measurement was about 2% based on several repeated measurements over the smooth surface. The absolute pressure inside the loop was measured by another pressure transducer (Validyne 0.5 psi diaphragm) and maintained below the atmospheric pressure at 97 kPa. The pressure drop measurement over the current SHS showed negligible DR when the test-section pressure was equal to or larger than the atmospheric pressure. As observed in previous experiments of Lei *et al.* (2009), Ling *et al.* (2016), and Gose *et al.* (2018), high pressure can push the air layer into the cavities of the SHS and expose the peaks of the roughness elements to the turbulent flow, reducing the DR performance of the SHS. Ling *et al.* (2016) carried out experiments over a SHS at two different hydrostatic pressures (98 kPa and 122 kPa). They concluded that the air layer over the SHS is compressed inside the roughness elements at the higher pressure while it is maintained at the lower pressure. Recently, the shadowgraphy particle tracking velocimetry measurement of Reholon & Ghaemi (2018) was carried out in atmospheric

pressure on a body-of-revolution sprayed with a superhydrophobic coating. They showed that the air layer over the SHS at the tested hydrostatic pressure was relatively flat and covering all the roughness elements except the large roughness peaks which are exposed to the flow.

The experiments were operated at a constant flow rate with a bulk velocity of $U_b = 0.93$ m/s, defined as the average velocity over the cross-section. The Reynolds number is $Re_b = 7,000$, defined as $Re_b = U_b H / \nu$, with ν denoting the kinematic viscosity equal to 8.02×10^{-7} m²/s. The friction velocity over the no-slip smooth surface is $u_{\tau 0} = 0.060$ m/s and the wall unit is $\lambda_0 = 13.3$ μ m, based on the wall-normal gradient of mean velocity in the linear viscous sublayer as described in subsection 3.1. The estimation also agrees with the inner scaling obtained from Clauser's method using the logarithmic law of the turbulent boundary layer (Clauser 1956). The friction Reynolds number is $Re_\tau = 225$, defined as $Re_\tau = u_\tau H / (2\nu)$. The components of the instantaneous velocity vector are shown by U , V , and W , and the components of the fluctuating velocity by u , v , and w in the x , y , and z directions, respectively. A summary of the channel flow parameters is listed in Table 1.

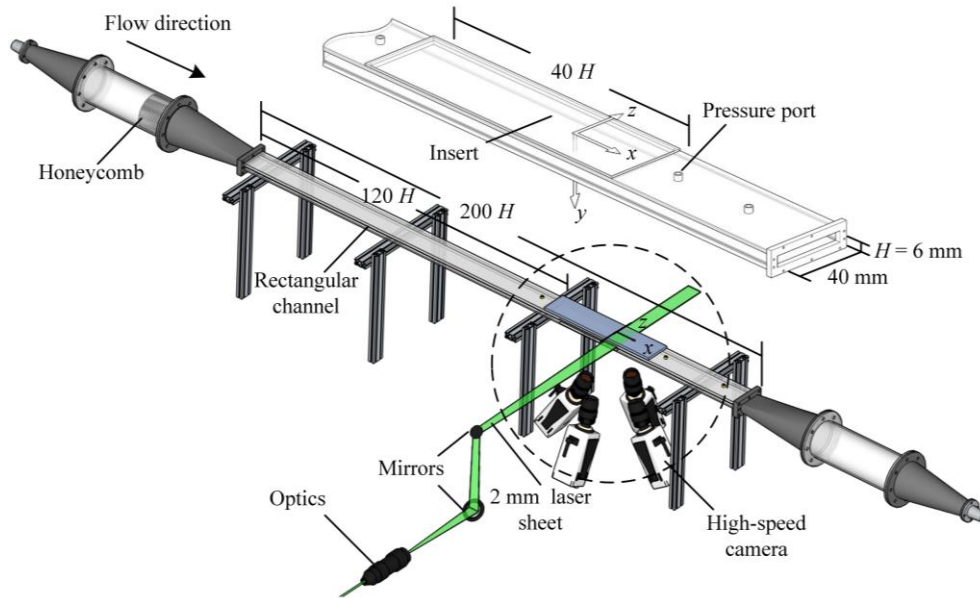


FIGURE 1. Schematic of the experimental set-up showing the rectangular channel, the camera arrangement, and the illumination path for the 3D-PTV experiment. The inset shows a closer view of the test section and the replaceable insert to mount the SHS.

2.2 Superhydrophobic surface

A SHS with a random texture was coated on the insert module using a commercial spray coating (Rust-Oleum NeverWet). This module has dimensions of 240 mm ($40H$) and 40 mm in the x and z -direction and was installed flush with the top wall 720 mm ($120H$) downstream from the channel entrance as seen in figure 1. This spray coating was used in previous experiments (Aljallis et al. 2013; Zhang et al. 2015; Vajdi Hokmabad & Ghaemi 2016; Abu Rowin *et al.* 2018) and is applied in two steps. First, a layer of base coat with no particles is sprayed to increase the adhesion of the surface. In the second step, a layer of particles is sprayed which consists of 5 μ m up to 30 μ m particles diameter as can be seen in the scanning electron microscopy (SEM) images of figure 2. Contact angle measurements were performed by characterizing the three-phase contact line using the Young Laplace fitting method (Young 1805). Measurements were carried out using a droplet shape analyzer (DSA-100 KRÜSS GmbH) by placing a 10 μ L droplet at 3 locations over eight

superhydrophobic surfaces. The surfaces had an average contact angle of 152° with a standard deviation of 2.2° . The contact angle hysteresis was 2.8° with a standard deviation of 1.8° , estimated as the difference between the advancing and receding contact angles. The roll-off angle over the current SHS was relatively small and equal to 1.4° with a standard deviation of 0.6° .

Parameter	Dimensions	Value
U_b	m/s	0.93
Re_b	-	7,000
$u_{\tau 0}$	m/s	0.058
λ_0	μm	13.8
Re_τ	-	217

TABLE 1. Summary of the parameters of the turbulent channel flow with smooth walls.

A step profiler (XP-300, Ambios Technology, USA) with $2.5 \mu\text{m}$ stylus tip radius and $30 \mu\text{m/s}$ scanning speed was used to measure the variation of the SHS roughness heights as shown in figure 2(c). The measurement uncertainty was estimated to be about $0.1 \mu\text{m}$ based on measurement on a microscope slide (i.e. flat surface). The stylus force was set to 1 mg since higher forces resulted in scratching the surface and peeling the hydrophobic coating. The surface roughness, R , in figure 2(c) appears to have different peak heights up to about $20 \mu\text{m}$. The root-mean-square of surface roughness (R_{rms}) was 4.9 with a standard deviation of $0.3 \mu\text{m}$ based on measurements at different locations on eight superhydrophobic surfaces. The normalized roughness using the wall unit of the flow over the SHS is $k^+ = R_{rms}/\lambda = 0.35$, where $\lambda = 17 \mu\text{m}$. The average texture width, g , between the peaks with $R > 3 \mu\text{m}$ is $85 \mu\text{m}$, which is equivalent to $g^+ = 5.0\lambda$. The profilometer measurement over a longer distance of 120 mm is also shown in figure 2(d) to characterize the low wave-number features. The mean distance between roughness peaks (d_p) which are larger than a prescribed threshold is illustrated in figure 2(d). As it can be seen, d_p increases with the increase of the roughness height and reaches up to a d_p of 26 mm for the largest roughness peaks with $R = 22 \mu\text{m}$. The plastron visualization of Reholon & Ghaemi (2018), over a SHS with a similar structure under turbulent flow, has shown that at high DR ($>15\%$) a relatively flat air plastron covers the surface roughness. At lower DR, the surface elements are exposed to the liquid flow and a rough interface forms.

2.3 Time-resolved 3D particle tracking velocimetry

Time-resolved 3D-PTV was used to measure the trajectory of tracer particles in a three-dimensional volume covering the inner layer over the test surfaces. The applied Lagrangian particle tracking technique is based on the shake-the-box (STB) method of Schanz *et al.* (2013; 2016) and carried out in Davis 8.4 (LaVision GmbH). This method uses a combination of trajectory predictions and an image matching technique (shaking) based on the iterative particle reconstruction technique (IPR) of Wieneke (2012) to obtain an accurate estimation of particle position. The STB method can provide measurements with high spatial resolution in the vicinity of the wall ($y^+ \sim 1$) as shown previously by Schröder *et al.* (2015) and Novara *et al.* (2016).

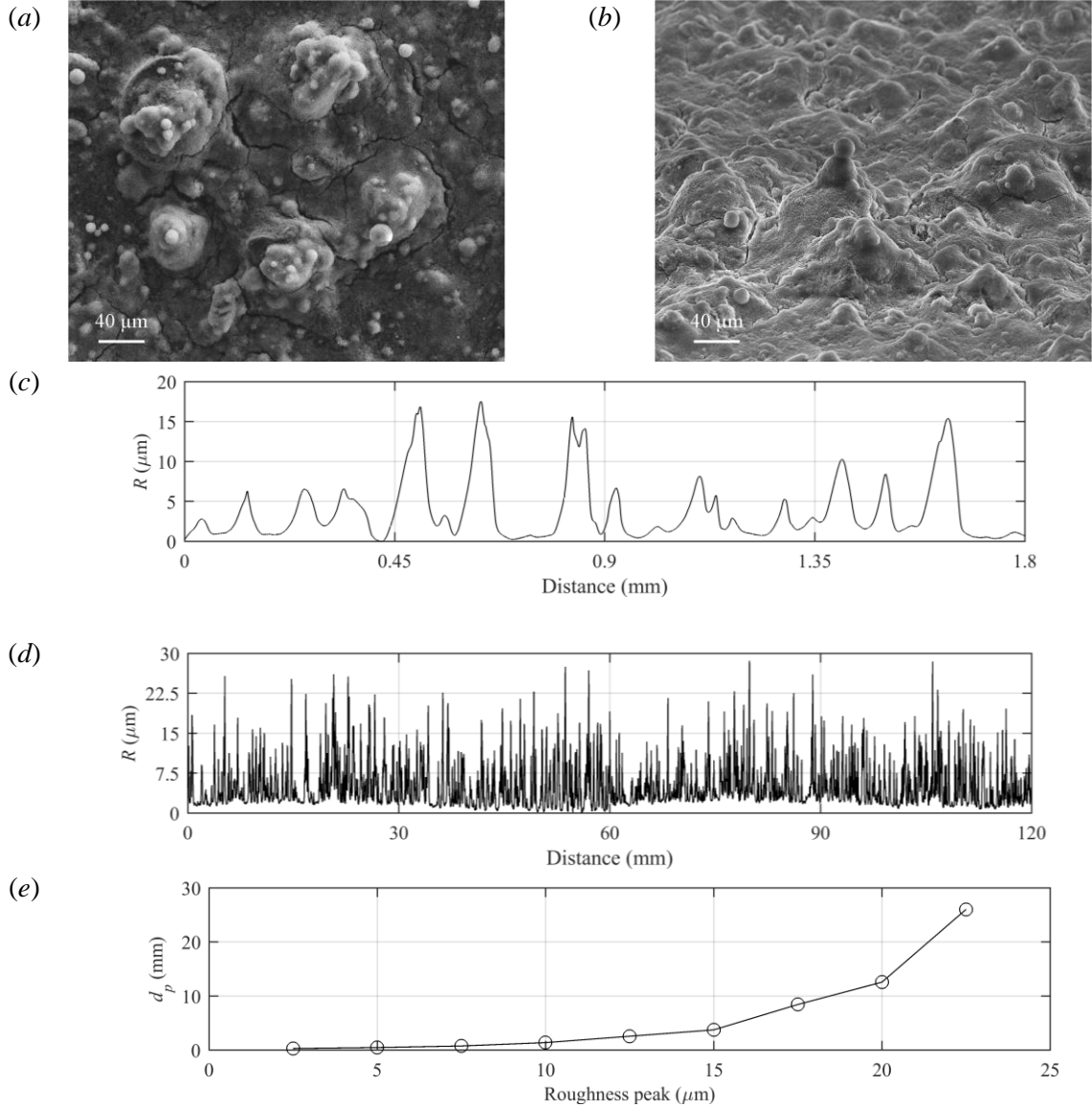


FIGURE 2. SEM images with (a) top-down and (b) tilted views at 65° of the randomly texture SHS. Samples of the profilometer measurement of microscale roughness of the SHS over (c) 1.8 mm and (d) 120 mm of the sample. (e) The mean distance between roughness peaks.

The imaging system consisted of four high-speed Phantom v611 cameras with a CMOS sensor of 1280×800 pix. The CMOS sensor features $20 \times 20 \mu\text{m}^2$ pixels with 12-bit resolution. The cameras were arranged in a plus-like arrangement (Scarano 2012) as visualized in figure 1. The cameras were equipped with Scheimpflug adapters to align the depth-of-field with the laser sheet. Nikon 105 mm lenses with aperture settings of $f/22$ were used. The magnification and digital resolution of the imaging system were 0.56 and $35.5 \mu\text{m}/\text{pix}$, respectively. The solid viewing angle between the wall-normal axis and the cameras was between 25° and 30° . The illumination was provided by a dual-head Nd: YLF laser (DM20-527, Photonics Industries) with 20 mJ/pulse. Spherical and cylindrical lenses were used to form a collimated laser sheet. The lower edge of the laser sheet was cropped by a knife-edge filter while the upper edge of the laser sheet was cropped by the channel wall to ensure a top-hat intensity profile starting from the wall surface. The

cropping resulted in a final laser sheet thickness of 1.5 mm in the y -direction and 21 mm in the x -direction. The measurement volume was $21 \times 1.5 \times 21 \text{ mm}^3$ ($1522\lambda \times 108\lambda \times 1522\lambda$), which is equivalent to $596 \text{ pix} \times 43 \text{ pix} \times 596 \text{ pix}$ in the x , y , and z directions. The laser pulses and the four high-speed cameras were synchronized using a programmable timing unit (PTU X, LaVision GmbH) controlled by DaVis 8.2. Nine sets of 1,610 single-frame images were recorded at a frequency of 4 kHz. At this recording frequency, the maximum particle displacement was about 11 pixels. One of the challenges for particle image velocimetry and PTV over SHSs is caused by the reflection of the laser light from the roughness elements and the shiny air plastron. Thus, the flow loop was seeded with 10 μm red-fluorescent particles (polystyren PS-FluoRed-Fi225) that emit light at a wavelength of 607 nm when illuminated with 530 nm green light. The experiments used a small particle image density of 0.003 particles per pixel (ppp) at 2-3 particles/ mm^3 . This small particle image density is not a limitation of STB as the algorithm is capable of processing images with up to 0.075 ppp (Schanz *et al.* 2016). In the current experiment, the smaller particle image density was chosen due to the large amount of monodisperse fluorescent particles required to seed ~ 40 liters of water. As result, spatially uncorrelated data at low ppp was collected over a longer time to obtain statistical convergence. The Band-pass filters (# 1108573, LaVision) with wavelength limits of 545 to 800 nm were attached to each camera to only record the emitted light by the fluorescent.

A 2D calibration target with 2 mm spaced holes was utilized for the initial calibration of the four cameras. The target was moved twice with 1 mm increments in the y -direction by a micrometer traverse resulting in three parallel planes. The mapping function between the image and the physical three-dimensional space was carried out using a pinhole model. Due to small movements of the test section and a relatively large magnification, a large initial distortion of about 2-3 pixels was seen in the disparity map. The volume self-calibration (VSC) algorithm of Wieneke (2008) was applied to reduce the residual root-mean-square to about 0.02 pixels.

The minimum intensity of images was subtracted from each image followed by normalization using the average image to increase the signal-to-noise ratio. The images were further improved by applying local intensity normalization over a window with a kernel of 10 pixels, and a Gaussian smoothing with a kernel of 3×3 pixels was used to avoid any peak locking (Kähler *et al.* 2012). An optical transfer function (OTF) was obtained and used for every iterative particle reconstruction step and the shaking algorithm as described by Schanz *et al.* (2012). We limited the largest particle shift between two successive image frames to 13 pixels and allowed a maximum triangulation error of 0.5 pixels. Particles closer than 1 pixel were eliminated to prevent any erroneous particle trajectories. The wall location was obtained using the minimum intensity of the ensemble of images, which includes a few surface glares points. The minimum image is reconstructed into a 3D domain using the multiplicative algebraic reconstruction technique (MART) to obtain the 3D location of the surface glares. The intensity of the reconstructed glare points is summed along the x and z -directions and fitted with a Gaussian distribution to obtain the wall location with sub-pixel accuracy. The estimated uncertainty of the Gaussian fit is 0.1 pix, equivalent to $0.26\lambda_0$.

To reduce the noise of particle trajectories and obtain the Lagrangian velocity and acceleration, polynomials with different orders and different kernel sizes can be fitted on the measured particle position. Gesemann *et al.* (2016) applied a B-spline regression for noise reduction of STB data. Their regression method optimized the B-spline using a cost function assuming that the third derivative of particle position with respect to time (jolt) has a white noise distribution. In the current investigation, we applied a simpler method using a second-order polynomial fitted to each

component of particle location (i.e. x , y , and z). The optimum polynomial kernel size is also based on the root-mean-square of acceleration (a_{rms}^+) as suggested by Voth *et al.* (2002).

In figure 3(a), a_{rms}^+ is estimated at different wall-normal locations for a wide range of kernel sizes, shown in time steps of $\Delta t = 250 \mu s$. According to Voth *et al.* (2002), an initial linear increase of a_{rms}^+ (in a semi-log presentation) should be observed when the kernel size reduces. As the kernel further reduces to a certain limit, a_{rms}^+ rapidly increases and deviates from the linear trend. The kernel size (t_k) at which a_{rms}^+ deviates by 10% from the linear trend is selected as the optimum kernel. For instance, in figure 3(a), a_{rms}^+ at $y^+ = 70$ follows a linear trend until t_k reduces to 25-time steps. The optimum t_k is estimated for different wall-normal locations and is presented in figure 3(b). The optimum size varies from $t_k = 70$ time steps ($70 \times 250 \mu s$) at $y^+ = 10$ to $t_k = 25$ time steps ($25 \times 250 \mu s$) at $y^+ = 70$.

It is important to note that there is a steep wall-normal velocity gradient; the near-wall particles move by ~ 1 pixel ($\sim 2u_\tau$ at $y^+ = 2$) while the particles away from the wall move up to 11 pixels between two consecutive image frames ($\Delta t = 250 \mu s$). Therefore, more time steps are required for the near-wall particles to have a similar displacement (i.e. kernel length in pix or mm) as the faster particles away from the wall.

At each wall-normal location, the trajectories which are shorter than the optimum t_k were discarded. The effect of the filter is evaluated using spectra of particle position (Appendix section) and by comparing the measured Reynolds stresses over the smooth channel with the DNS of Gilbert & Kleiser (1991) and Rastegari & Akhavan (2015).

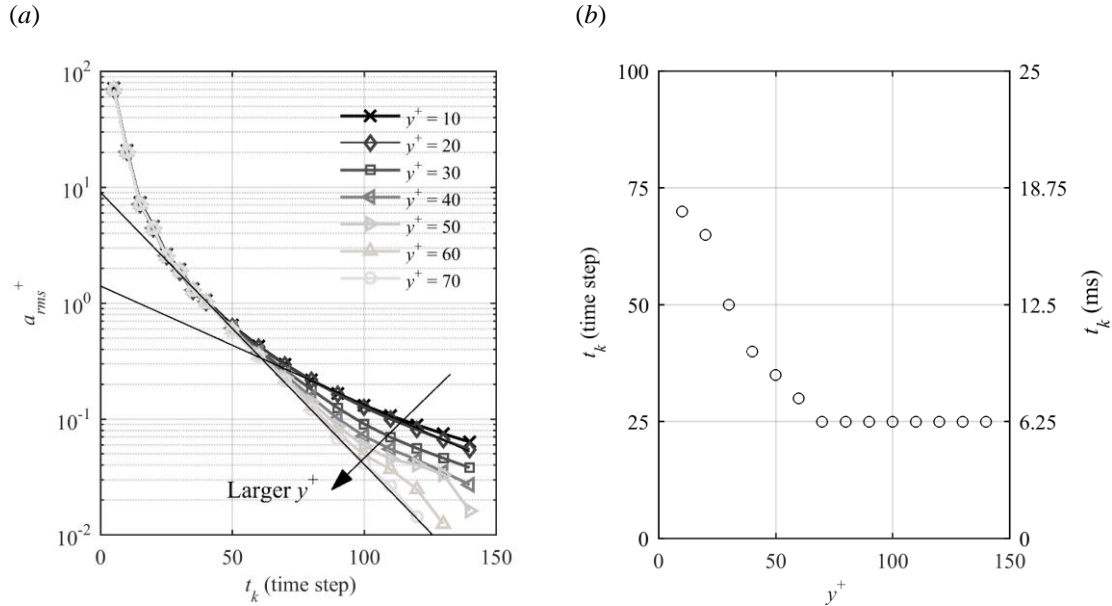


FIGURE 3. (a) Variation of a_{rms}^+ with kernel size (t_k) at different wall-normal locations. The solid black lines is fitted to $y^+ = 10$ and 70 data, showing that the a_{rms}^+ estimation deviates from the linear model at $t_k = 70$ and 25 , respectively. (b) The estimated optimum t_k in time steps (left axis) and in milliseconds (right axis).

The x , y , and z components of a trajectory before and after applying the second-order polynomial filter are shown in figure 4. The trajectory is at average wall-normal locations of $y = 0.16$ mm (12λ) with t_k of 60. As shown in figure 4(a), the raw trajectory in the x direction is smooth and the regression filter has a negligible effect. The trajectory in the y direction is relatively noisy in figure 4(b) as it is the out-of-plane motion for the cameras. However, the second-order polynomial filter can capture the motion and reduce the noise. The trajectory in the

z direction in figure 4(c) has relatively low negligible noise compared with the y component. However, the second-order polynomial filter also captured the motion and reduce the noise. The velocity of the particle is obtained from the coefficient of the second-order polynomial in the central part of the trajectory, where the full t_k can be applied. This central part is shown with a solid line in figure 4. Evaluation of the random noise of the current 3D-PTV measurement for each component using the statistical convergence of the data is included in the Appendix section. The analysis shows that the random noise was minimal for the velocity profiles and limited to 0.60% of the mean value at $y^+ = 15$. However, the convergence analysis of Reynolds stresses showed a higher level of random noise which reached up to 0.91 % of $\langle w^2 \rangle$ at $y^+ = 15$ over the smooth surface.

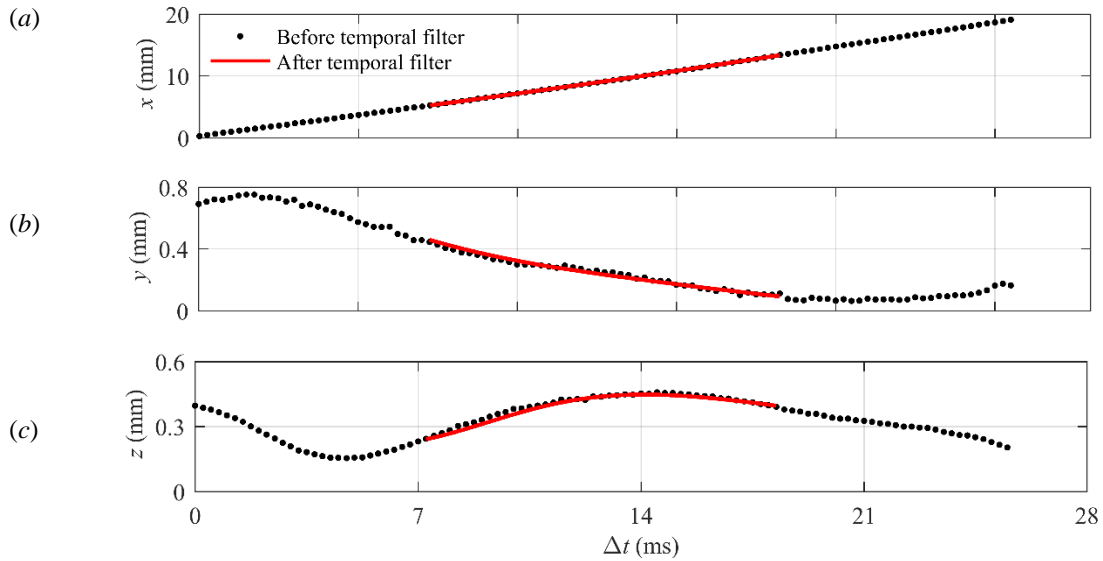


FIGURE 4. A particle trajectory before and after applying the regression in the (a) x , (b) y and (c) z directions. The trajectory is at an average wall-normal location of $y = 0.16$ mm.

3. Results and Discussion

The streamwise and spanwise velocities and the Reynolds stresses over the SHS are investigated in this section. The test surfaces are placed at the top wall of the channel where $y = 0$. The DNS results of smooth channel flow from Gilbert & Kleiser (1991) at $Re_\tau = 211$ and Rastegari & Akhavan (2015) at $Re_\tau = 222$ are also used to evaluate the uncertainty in the measurement of velocity and Reynolds stresses. The superscript $+$ denotes parameters normalized using inner scaling, i.e. velocities are normalized by u_τ and the coordinate system is normalized by λ . If the subscript 0 is added, it indicates that the parameters are normalized using the inner scaling of flow over the smooth surface. When there is no subscript, the normalization is carried out by the inner scaling of the corresponding surface.

3.1 Streamwise velocity

Scatter plots of the streamwise velocity of the particles over the smooth and SHS from 3D-PTV are shown in figures 4(a) and 4(b), respectively. The velocity over both surfaces is normalized using the inner scaling of the smooth surface ($U^+_0 = U/u_{\tau 0}$), and the plots cover the inner layer up to $y^+ = 100$. The mean velocity profile is also shown using the solid lines by averaging the data over $10 \mu\text{m}$ (0.72λ) bins with 75% overlap. The mean velocity profile at $y^+ < 2.5$ is not shown due

to its deviation from the expected linear viscous sublayer profile $\langle U \rangle^+ = y^+$ for the smooth surface. Therefore, $y^+ = 2.5$ is considered as the lower limit of the measurements. This limitation is imposed by the size of the fluorescent tracer particles ($d = 10 \mu\text{m} = 0.72 \lambda$) and lack of data at $y^+ < 2.5$.

As shown in figure 5(a), there are a large number of particles with small U_0^+ (< 2.5) in the immediate vicinity of the smooth wall, indicating the no-slip boundary condition. However, particles with larger U_0^+ varying from 2 to 8 (0.12 to 0.48 m/s) are observed at the lowest wall-normal limit of the measurement in figure 5(b). The larger streamwise velocity at $y^+=2.5$ indicates the presence of a streamwise slip velocity at the SHS. The larger scatter of the instantaneous streamwise velocity in the vicinity of the SHS also agrees with the 2D-PTV of Abu Rowin *et al.* (2017) over a SHS at $Re_\tau = 140$.

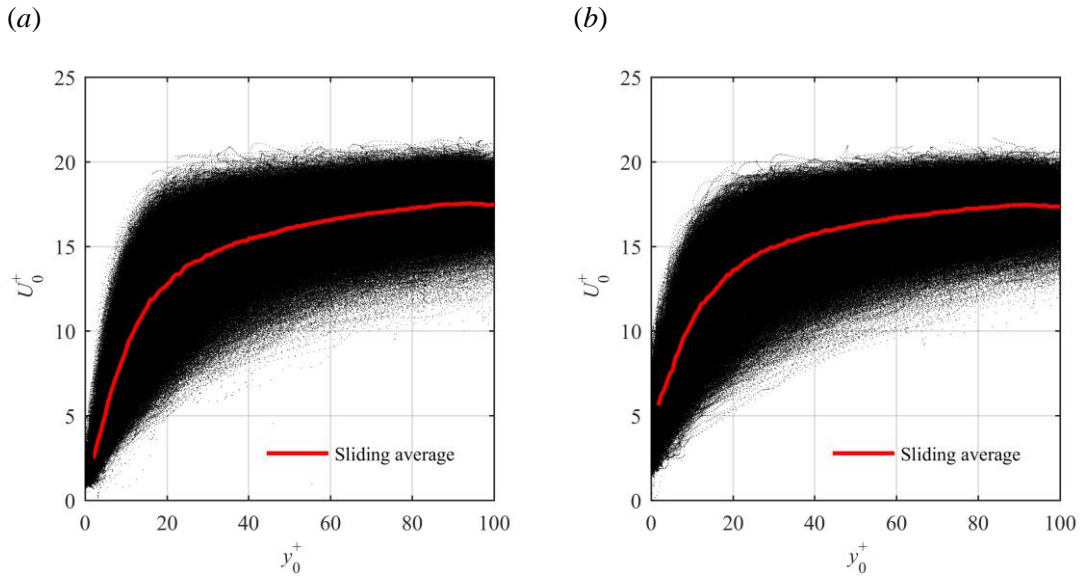


FIGURE 5. Streamwise velocity of the individual tracers over (a) smooth and (b) SHS. The data is normalized using inner variables of the smooth surface.

The mean streamwise velocity at $y^+ < 15$ over the smooth and SHS are presented in figure 6. The inner variables over the smooth surface are estimated using the wall-normal gradient of $\langle U \rangle$ within $2.5 < y^+ < 3.5$. Figure 6(a) shows that the mean streamwise velocity over the smooth surface follows the law-of-the-wall ($y^+ = \langle U \rangle^+$) in the linear viscous sublayer and the DNS of Rastegari & Akhavan (2015) over the smooth channel at $Re_\tau = 222$. The extrapolation of the fitted line on the velocity profile of the smooth surface approaches zero at the wall. The values of $\langle U \rangle_0^+$ over the SHS are higher than those of $\langle U \rangle_0^+$ over the smooth surface near the wall region due to the streamwise slip velocity. Farther away from the wall, the mean velocity over the SHS becomes smaller than the smooth surface; however, the outer layer is not shown for brevity. The numerical simulation of Min & Kim (2004), the theoretical work of Fukagata *et al.* (2006), and measurements of Abu Rowin *et al.* (2017) have also observed a larger near-wall velocity and a smaller velocity farther away from a SHS. The slip velocity over the SHS is estimated by extrapolation of a linear fit over the near-wall velocity within $2.5 < y^+ < 3.5$ to $y^+ = 0$ as shown in figure 6(a). The estimated slip velocity is $U_{s0}^+ = U_s/u_{\tau 0} \approx 4.54$ ($U_s = 0.27$ m/s), which results in $U_s/U_b \approx 30\%$. The repeatability of the measurement is confirmed by carrying out the STB measurements over two additional SHSs manufactured through a similar spray coating procedure.

The measured U_s over these two SHSs is 0.30, and 0.25 m/s, showing $\pm 8\%$ variation. The slope of this line is also used to estimate the inner scaling over the SHS. The estimated friction velocity over the SHS is $u_\tau = 0.048$ m/s, which is reduced by 17% with respect to the smooth surface. This corresponds to $Re_\tau = 180$ over the SHS. In figure 6(b), the velocity over the smooth and SHS is normalized by their corresponding inner scaling. The fitted line over the mean velocity of the SHS within $2.5 < y^+ < 3.5$ follows $\langle U \rangle^+ = y^+ + U_s^+$. The slip velocity normalized as $U_s^+ = U_s/u_\tau$ is 5.76, and the slip length is $l_s \approx 96.5 \mu\text{m}$ (5.91λ).

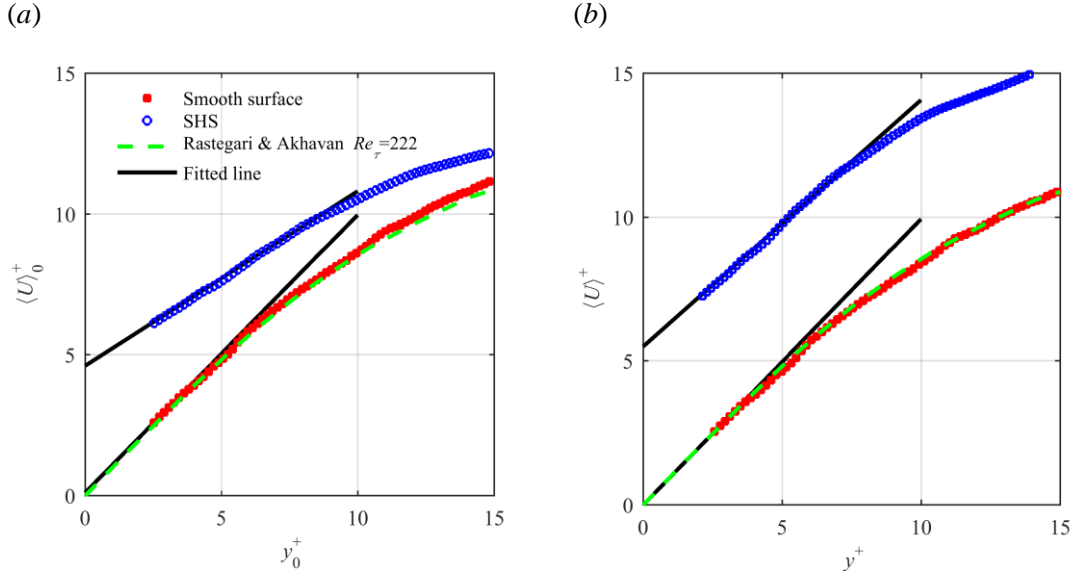


FIGURE 6. Mean velocity profiles normalized by the inner variables of the (a) smooth surface and (b) their corresponding inner variables. The mean values are obtained over bins of $10 \mu\text{m}$ (0.72λ) with 75% overlap in y direction. The fitted lines over the data of $2.5 < y^+ < 3.5$ are shown with black solid line. The DNS of Rastegari & Akhavan (2015) at $Re_\tau = 222$ is also shown for comparison.

The probability density function (PDF) of U_0^+ over the smooth and SHS in the immediate vicinity of the wall at $2.5 < y^+ < 3.5$ is shown in figure 7(a). This PDF shows that the SHS has shifted the streamwise velocity distribution toward larger velocities with a broader distribution due to the streamwise slip velocity. Farther away from the wall at $45 < y^+ < 46$, the streamwise slip has a smaller influence on the PDF of U_0^+ as shown in figure 7(b). Our investigation of different wall-normal locations within the log-layer shows a similar trend: a slightly narrower PDF for the SHS. The larger mean streamwise velocity and the wider PDF for $2.5 < y^+ < 3.5$ is consistent with the larger near-wall $\langle u^2 \rangle$ observed in the numerical simulation of Min & Kim (2004) and Rastegari & Akhavan (2015).

For the analysis of streamwise velocity over a wider wall-normal distance, semi-logarithmic presentations of $\langle U \rangle^+$ over the smooth and SHS are plotted in figure 8(a), together with the DNS of Rastegari & Akhavan (2015). The data is normalized using the inner scaling of the corresponding surface obtained from the linear velocity gradient in figure 6(a). The law-of-the-wall for the linear viscous sublayer as $\langle U \rangle^+ = y^+$ and the log-law expressed as $\langle U \rangle^+ = 1/\kappa \ln y^+ + B$ are also shown with the von Kármán constant of $\kappa = 0.41$ and $B = 5.2$. The profile of the smooth surface agrees with the law-of-the-wall and the log-law, indicating a fully developed channel flow (Kim *et al.* 1987). The 3D-PTV measurements are also consistent with the DNS profile in the buffer layer range of $5 < y^+ < 30$. The $\langle U \rangle^+$ of the SHS does not follow the standard log-law and is shifted upward due to the slip velocity. The upward shift of $\langle U \rangle^+$ in the semi-logarithmic

representation over a SHS has been observed in previous numerical simulations (e.g., Min & Kim 2004; Martell *et al.* 2010) and experiments (Woolford *et al.* 2009; Ling *et al.* 2016; Abu Rowin *et al.* 2017).

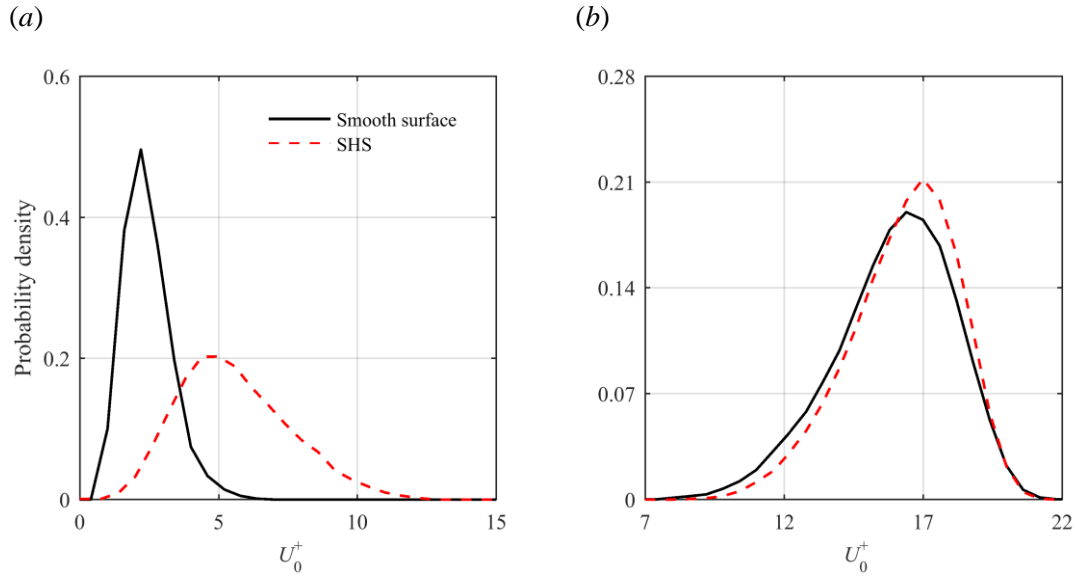


FIGURE 7. Probability density functions of streamwise velocity over the smooth and SHS normalized by the inner variables of the smooth wall for data within (a) $2.5 < y^+ < 3.5$, and (b) $45 < y^+ < 46$.

In figure 8(b), the slip velocity is subtracted from the mean velocity profile (i.e. $\langle U \rangle^+ - U_s^+$). As a result, the velocity profile over the SHS overlaps with the velocity profile over the smooth surface in the linear viscous sublayer for $y^+ < 3.5$. In the buffer and log layers, the SHS velocity profile appears to have a slight downward shift. A similar downward shift was reported in the DNS of Min & Kim (2004) when they imposed a slip velocity at the wall in both directions (l_x and l_z). Thus, the downward shift of the log-law in figure 8(b) indicates the presence of both streamwise and spanwise slip over the current SHS.

3.2 Spanwise velocity

Scatter plots of the spanwise particle velocity over the smooth and SHS are presented in figure 9(a) and (b), respectively. The velocity over both surfaces is normalized using the inner scaling of the smooth surface. The mean of absolute spanwise velocity (i.e. $\langle W \rangle_0^+ = \langle |W| \rangle / u_{\tau 0}$) is also presented with a solid line from an averaging process over windows of $30 \mu\text{m}$ (2.2λ) with 75% overlap in the y -direction. The lower limit of the mean spanwise velocity is also set to $y^+ = 2.5$, similar to the mean streamwise velocity. Due to the no-slip condition, the spanwise velocity in the vicinity of the smooth surface is negligible in figure 9(a). In contrast, a large number of tracers with a finite spanwise velocity within $-0.8 < W_0^+ < 0.8$ appear in the immediate vicinity of the SHS in figure 9(b). This large scatter of spanwise velocity confirms the presence of a spanwise slip velocity (W_s). A narrower band of scattering in W_0^+ is observed away from the wall ($y^+ > 20$) in figure 9(b) when compared with the smooth surface in figure 9(a). This will be further scrutinized by investigating profiles of $\langle w^2 \rangle$ in the next section.

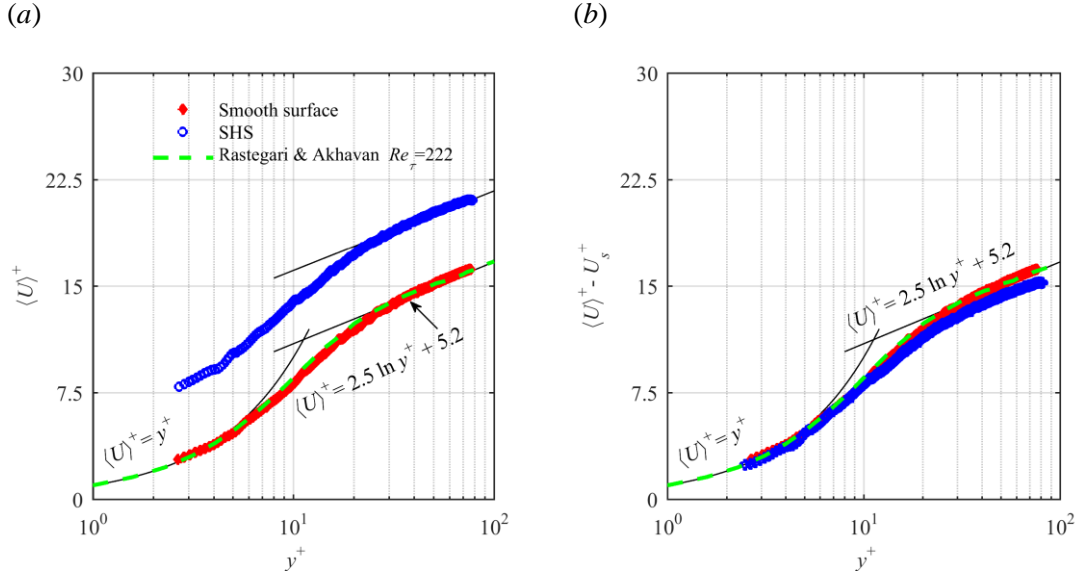


FIGURE 8. (a) Semi-logarithmic plots of mean streamwise velocity normalized with the inner scaling of the corresponding surface $\langle U \rangle^+$. (b) Semi-logarithmic plots of $\langle U \rangle^+ - U_s^+$. The DNS of Rastegari & Akhavan (2015) in a smooth channel at $Re_\tau = 222$ is also shown for comparison.

The profiles of $\langle W \rangle_0^+ = \langle |W| \rangle / u_{\tau 0}$ over the smooth and SHS are shown in figure 10(a). The magnitude of $\langle W \rangle_0^+$ is much smaller than $\langle U \rangle_0^+$; $\langle W \rangle_0^+$ is about $0.4u_{\tau 0}$ at $y^+ = 5$ while $\langle U \rangle_0^+$ is $5u_{\tau 0}$ at $y^+ = 5$. The profile of $\langle W \rangle_0^+$ also does not follow a linear trend in the viscous sublayer. The values of $\langle W \rangle_0^+$ over the smooth surface tend toward a negligible velocity at the wall, confirming the no-slip boundary condition. The profile of $\langle W \rangle_0^+$ over the SHS is shifted upward and approaches a finite value at the wall, indicating a slip velocity in the spanwise direction. Further away from the SHS at $y^+ > 10$, $\langle W \rangle_0^+$ becomes smaller than that of the smooth surface. This trend is consistent with the streamwise velocity profile but the crossing point is closer to the wall due to the smaller spanwise slip velocity. The profiles of mean absolute spanwise velocity normalized with their corresponding inner scaling, $\langle W \rangle^+ = \langle |W| \rangle / u_\tau$, are shown in figure 10(b). It is observed in this figure that the variation of $\langle W \rangle_0^+$ can be described by a second-order polynomial. The extrapolation of the second-order polynomial within $2.5 < y^+ < 7$ for the smooth surface to $y^+ = 0$ also results in zero $\langle W \rangle_0^+$, which agrees with the no-slip boundary condition. Thus, the spanwise slip velocity and length over the SHS are estimated by applying a second-order polynomial to the data within $2.5 < y^+ < 7$. As displayed in figure 10(b), the extrapolation of this model results in a spanwise slip velocity of $0.38u_\tau$ (0.018 m/s) over the SHS which corresponds to an effective spanwise slip length of 5.86λ ($l_z \approx 95.8 \mu\text{m}$).

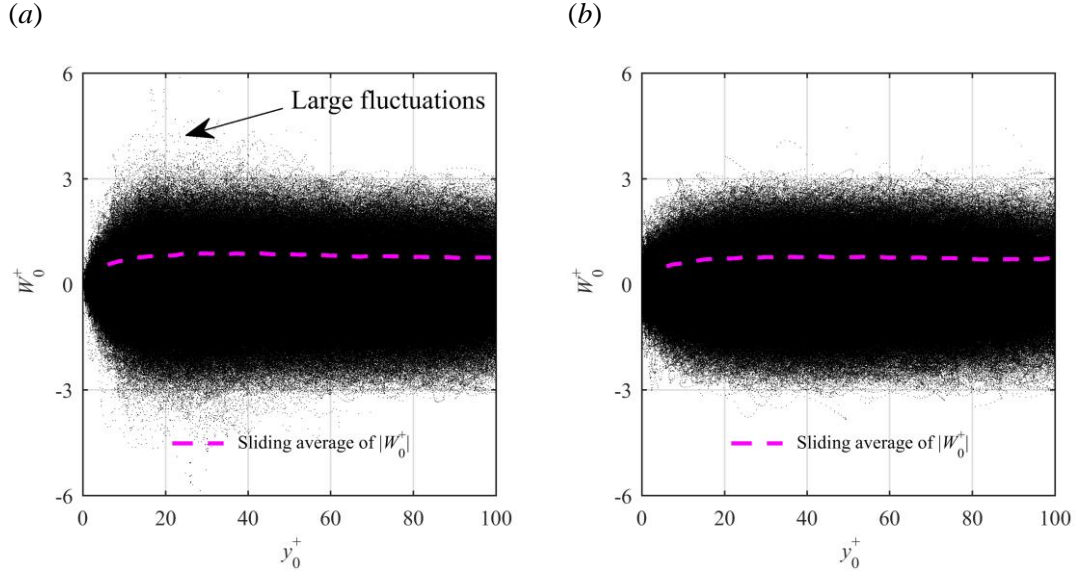


FIGURE 9. Spanwise velocity of the tracers over the (a) smooth and (b) SHS normalized by the inner scaling of the smooth surface. The dashed line shows the mean of the absolute value of spanwise velocity, $\langle |W| \rangle / u_{\tau 0}$, obtained by averaging in $30 \mu\text{m}$ (2.2λ) bins with 75% overlap.

The magnitude of the slip length in the streamwise direction ($l_x = 96.3 \mu\text{m} \approx 5.9\lambda$) is comparable to the magnitude of the slip length in the spanwise direction ($l_z = 95.8 \mu\text{m} \approx 5.9\lambda$). Therefore the slip boundary condition over the current randomly textured SHS with $k^+ = 0.35$ and $g^+ = 6$ is isotropic. The results confirm the DNS of Seo & Mani (2018), in which a randomly patterned SHS with texture width of $g^+ = 4.3$ was modeled assuming a homogenized isotropic slip length ($l_x = l_z$). They observed that a SHS with a larger texture width $g^+ = 28.5$ cannot be modeled by an isotropic slip length model.

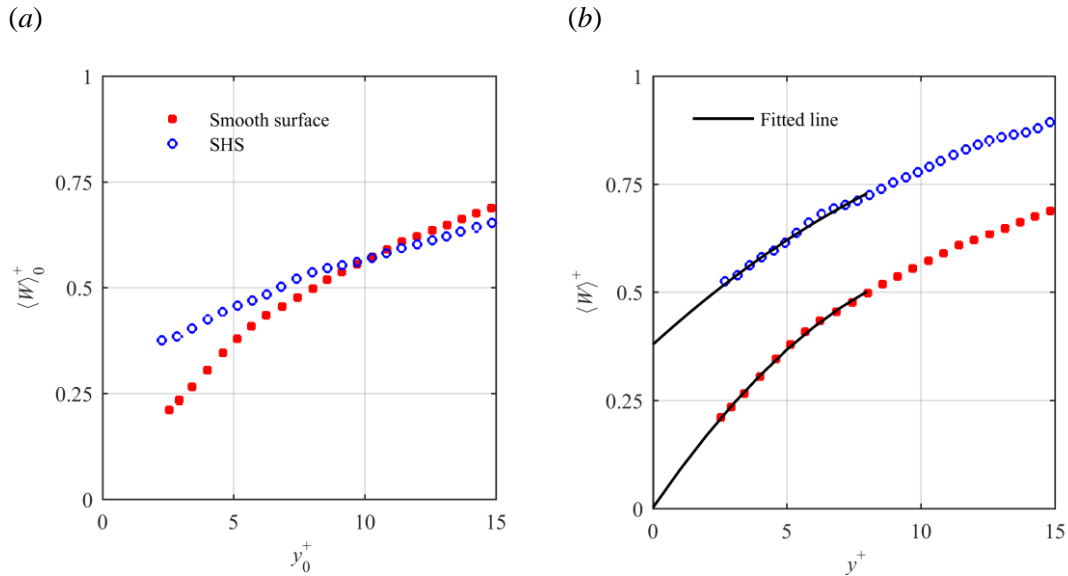


FIGURE 10. Mean of the absolute spanwise velocity over the smooth and SHS obtained from averaging over $30 \mu\text{m}$ (2.2λ) bins with 75% overlap. The values are normalized by (a) the inner variables of the smooth surface and (b) the corresponding inner variables. Second-order polynomials with $\langle W \rangle^+ = -0.0035y^{+2} + 0.0905y^+ + 0.0031$ and $\langle W \rangle^+ = -0.0015y^{+2} + 0.0560y^+ + 0.3800$ are applied to the smooth and SHS profiles, respectively.

The PDF of spanwise velocity over the smooth and the SHS for data within $2.5 \leq y^+ \leq 3.5$ and $45 \leq y^+ \leq 46$ are shown in figure 11(a) and 11(b), respectively. The SHS increases the probability of large spanwise velocity and reduces the probability of the slow spanwise velocity within $2.5 \leq y^+ \leq 3.5$. The effect reduces further away from the wall and the two PDFs overlap in figure 11(b). The DNS of Min & Kim (2004) also showed that an imposed l_z at the wall (without l_x) increases $\langle w^2 \rangle$ over an extended wall-normal distance; however, imposing both l_x and l_z results in a larger $\langle w^2 \rangle$ only at a short wall-normal distance. The latter is due to an increase of turbulence by the spanwise slip.

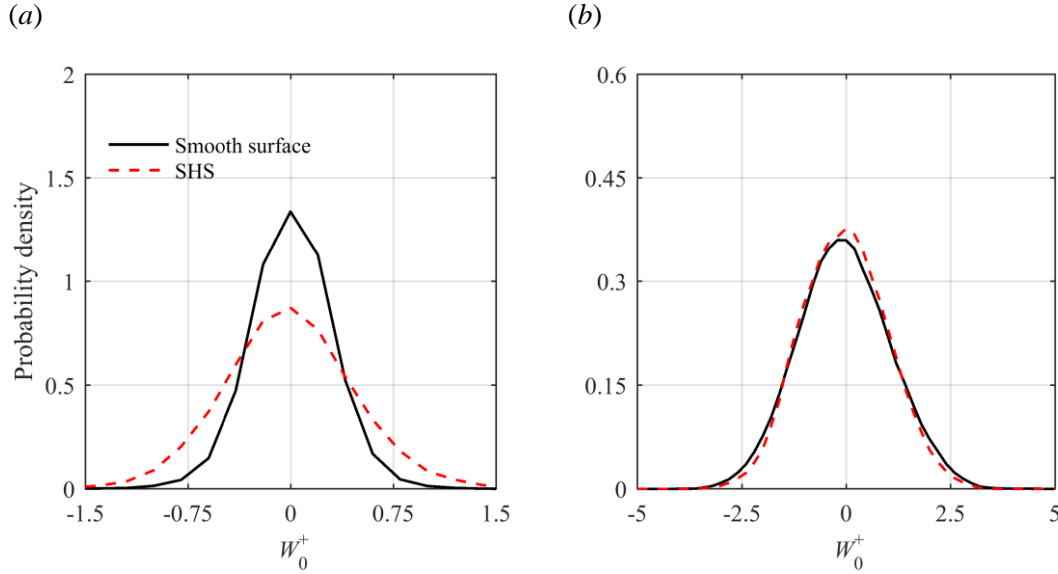


FIGURE 11. The probability density functions of spanwise velocity for velocity data within (a) $2.5 < y^+ < 3.5$ and (b) $45 < y^+ < 46$.

3.3 Turbulence statistics

The profiles of the non-zero components of the Reynolds stress tensors over the smooth and SHS from 3D-PTV at $y^+ < 60$ are shown in figure 12. Reynolds stresses in figure 12 are only shown at $y^+ < 60$ due to the lack of statistical convergence and larger error in Reynolds stresses close to upper boundary of 3D-PTV domain. The results from the DNS of Gilbert & Kleiser (1991) at a Re_τ of 211 and Rastegari & Akhavan (2015) at a Re_τ of 222 over the smooth surface are also shown for comparison. The two DNS data are also used to show the effect of a small change in Re_τ since the smooth surface is at a Re_τ of 217 and the SHS is at a lower Re_τ of 180. Also, the DNS of Rastegari & Akhavan (2015) over a SHS modeled as an organized array of streamwise microgrooves with $U_s/U_b = 0.32$ and a DR of 33% is included in the right-side plots of figure 12 for comparison. The SHS performance of the DNS is similar to the current investigation where $U_s/U_b = 0.3$ and the DR is about 30% (discussed in Section 3.5). In addition, Reynolds stresses over a SHS with randomly distributed posts (with the same height) from DNS of Seo & Mani (2018) is also included in the right-side plots of figure 12. The simulated SHS of Seo & Mani (2018) has $U_{s0}^+ = 4.5$ similar to $U_{s0}^+ = 4.54$ of current SHS. The averaging is carried out using windows of $50 \mu\text{m}$ (3.8λ) with 75% overlap in the y -direction. The Reynolds stresses are normalized by the inner variables of the smooth surface (i.e. $\langle u_i u_j \rangle_0^+ = \langle u_i u_j \rangle / u_{\tau 0}^2$) in figure 12 (a, c, and g) at the left side and normalized using the inner variable of the corresponding surface (i.e. $\langle u_i u_j \rangle^+ = \langle u_i u_j \rangle / u_\tau^2$) in figure 12(b, d, f, and h) on the right side. When the Reynolds stresses of

the SHS are normalized with the inner scaling of the smooth surface it is possible to study their variation at a constant bulk flow rate without considering the change in friction velocity. Both normalizations have been applied in the literature.

The streamwise Reynolds stress of the smooth surface $\langle u^2 \rangle_0^+$, in figure 12(a) follows the DNS profiles. There is a slight difference which is associated with the difference in Re_τ and measurement noise. In the near wall region of $y^+ < 12$, $\langle u^2 \rangle_0^+$ over the SHS is larger than the smooth surface due to the streamwise slip. Away from the wall, $\langle u^2 \rangle_0^+$ attenuates and becomes smaller than the smooth surface. The closer distance of the $\langle u^2 \rangle_0^+$ peak to the wall suggests a thinner inner layer over the SHS. The $\langle u^2 \rangle_0^+$ peak is 16% smaller than the smooth surface and is shifted closer to the wall to $y^+ = 14$. The DNSs of Min & Kim (2004) and Busse & Sandham (2012) also reported an increase of $\langle u^2 \rangle_0^+$ in the immediate vicinity of the wall and a reduction of $\langle u^2 \rangle_0^+$ farther away from the wall when a finite l_x was imposed. Min & Kim (2004) also showed that the modulation of $\langle u^2 \rangle_0^+$ became negligible when l_x was reduced from 3.57λ to 0.36λ .

When $\langle u^2 \rangle$ of the SHS is normalized with its friction velocity in figure 12(b), $\langle u^2 \rangle^+$ of the SHS is larger than that of the smooth surface in the near-wall region and it slowly approaches $\langle u^2 \rangle^+$ of the smooth surface at about $y^+=45$. A smaller $\langle u^2 \rangle^+$ is observed for the SHSs of Rastegari & Akhavan (2015) and Seo & Mani (2018) relative the measurements over the SHS in figure 12(b). The $\langle u^2 \rangle^+$ gradually approaches the smooth surface with an increase of y^+ . The smaller $\langle u^2 \rangle^+$ of the DNS over the SHS compared with $\langle u^2 \rangle^+$ of the current investigation is associated with the uniform height of the roughness elements in simulations of Rastegari & Akhavan (2015) and Seo & Mani (2018). The roughness height of the random textured SHS in the current experiment varies spatially as seen in figure 2. However, both DNS and 3D-PTV measurements confirm a larger $\langle u^2 \rangle^+$ over the SHS relative to the smooth surface.

The wall-normal Reynolds stress, $\langle v^2 \rangle_0^+$, over the smooth surface in figure 12(c) also agrees with the DNS profiles. The profiles of $\langle v^2 \rangle_0^+$ over the SHS and the smooth surface in figure 12(c) both start from zero at the wall as expected due to the non-permeable boundary condition. The overlap of $\langle v^2 \rangle_0^+$ for the smooth and SHS at $y^+ < 10$ also suggests negligible oscillation and movement of the SHS plastron in the wall-normal direction. However, $\langle v^2 \rangle_0^+$ of the SHS is smaller than the smooth surface in the inner layer, indicating smaller turbulence over the SHS. A similar trend is also seen in the DNS of Min & Kim (2004) over a flat SHS and the measurement of Abu Rowin *et al.* (2017) over a SHS with a roughness of $k^+=0.11$. The DHM of Ling (2017) shows a larger $\langle v^2 \rangle_0^+$ at the near-wall region of $y^+ < 10$ for SHSs with k^+ values as large as 0.89. The normalization based on the inner scaling of the corresponding surface results in larger values of $\langle v^2 \rangle^+$ over the SHS with respect to the smooth surface in figure 12(d). The $\langle v^2 \rangle^+$ of the DNS of Rastegari & Akhavan (2015) over the SHS in figure 12(d) is also larger than $\langle v^2 \rangle^+$ of the smooth surface within $10 < y^+ < 30$. The $\langle v^2 \rangle^+$ from Seo & Mani (2018) overlaps with $\langle v^2 \rangle^+$ of 3D-PTV.

The spanwise component of normal Reynolds stress, $\langle w^2 \rangle_0^+$, over the smooth surface in figure 12(e) falls between the DNS profiles of Gilbert & Kleiser (1991) and Rastegari & Akhavan (2015). This is expected since the Re_τ of the current measurements falls between the Re_τ of Gilbert & Kleiser (1991) and Rastegari & Akhavan (2015). Figure 12(a) and 12(e) show that the SHS modifies $\langle w^2 \rangle$ similarly to $\langle u^2 \rangle$. In figure 12(e), a larger $\langle w^2 \rangle_0^+$ is observed over the SHS at $y^+ < 7$ due to the spanwise slip (W_s), followed by a smaller $\langle w^2 \rangle_0^+$ farther away from the wall. This is consistent with the DNS of Min & Kim (2004) and Busse & Sandham (2012). The crossing-point for $\langle w^2 \rangle_0^+$ is closer to the wall than for $\langle u^2 \rangle_0^+$ due to a smaller magnitude of W_s compared with U_s .

In figure 12(f), $\langle w^2 \rangle^+$ over the SHS is larger than the smooth surface across the measurement domain. A similar trend is observed for $\langle w^2 \rangle^+$ of Rastegari & Akhavan (2015) and Seo & Mani (2018) over the SHS in figure 12(f).

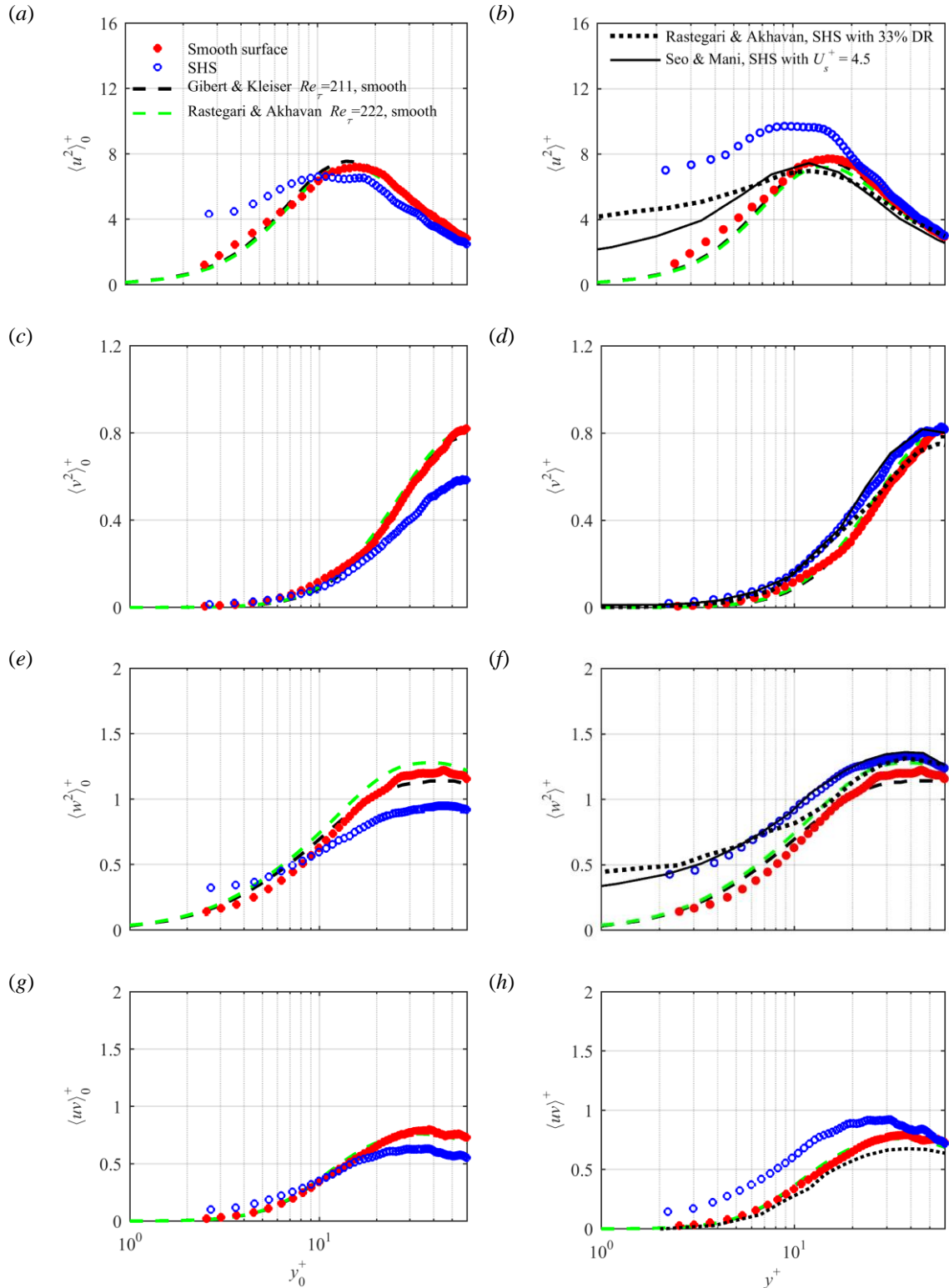


FIGURE 12. 3D-PTV measurement of (a, b) streamwise (c, d) wall-normal, (f) spanwise and (g, h) shear Reynolds stresses over the smooth and SHS. The Reynolds stresses normalized by the inner variables of

the smooth surface are denoted by $\langle u_i u_j \rangle_0^+$ in the left-side plots and those normalized by the corresponding inner variables are indicated by $\langle u_i u_j \rangle^+$ in the right-side plots.

The Reynolds shear stress in figure 12(g) overlaps with the DNS profiles. The $\langle uv \rangle_0^+$ of the SHS starts slightly larger than the smooth surface at $y^+ < 8$, while it is about 20% smaller farther away from the wall. This trend was previously observed by Ling (2017) and Abu Rowin *et al.* (2017). The level of increase in $\langle uv \rangle_0^+$ in the immediate vicinity of the SHS depends on the relative roughness of the SHS as discussed by Abu Rowin *et al.* (2017). Ling *et al.* (2016) noticed that $\langle uv \rangle_0^+$ over SHSs with large roughness ($k^+ > 1$) is larger than a smooth surface in both the inner and outer layer regions. In Figure 12(h), $\langle uv \rangle^+$ of the SHS is larger than the smooth surface and gradually approaches the smooth surface with an increase of y^+ . The $\langle uv \rangle^+$ profile from the DNS of Rastegari & Akhavan (2015) over the SHS in figure 12(h) follows the smooth surface. The low Reynolds shear stress of the DNS is associated with the assumed flatness of the SHS. The SHS simulated by Rastegari & Akhavan (2015) also results in a smaller $\langle uv \rangle^+$.

The distribution of viscous shear stress, $\tau_{v0}^+ = d\langle U \rangle_0^+ / dy_0^+$, Reynolds shear stress, $\tau_{R0}^+ = \langle uv \rangle_0^+$, and the total shear stress, τ_{t0}^+ , over the smooth and the SHS are shown in figure 13. The shear stresses are normalized by the wall shear stress of the smooth surface ($\tau_{w0} = \rho u_{\tau 0}^2$). Here ρ is the water density. It is observed that the viscous stress τ_{v0}^+ over the SHS is smaller than that over the smooth surface at $y^+ < 45$ due to the smaller wall-normal velocity gradient. Away from the wall, τ_{v0}^+ over the SHS overlaps with that over the smooth surface. The DHM measurement of Ling *et al.* (2016) also reported a similar trend of smaller τ_{v0}^+ over the SHS compared with the smooth counterpart. They observed that τ_{v0}^+ of the SHS approaches τ_{v0}^+ of the smooth surface at $y^+ = 50$. The Reynolds shear stress τ_{R0}^+ of the SHS is larger than the smooth surface at $y^+ < 10$, due to the larger streamwise velocity fluctuations as seen in figure 12(a). Farther from the wall, τ_{R0}^+ of the smooth surface rapidly increases and becomes larger than τ_{R0}^+ of the SHS surface. The total shear stress τ_{t0}^+ over the SHS is smaller than that over the smooth surface within the measurement domain. As expected, the τ_{t0}^+ of the smooth surface approaches one at the wall. Over the SHS, τ_{t0}^+ increase with y^+ and reaches a local maximum at about $y^+ = 15$. The increase of τ_{t0}^+ over the SHS in the near wall region is also observed in the experiment of Ling *et al.* (2016).

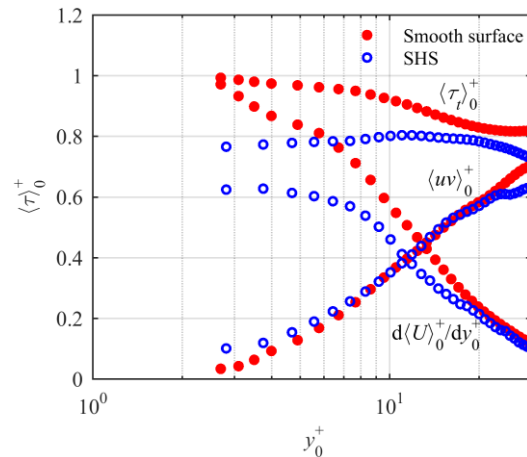


Figure 13. Profiles of viscous shear stress (τ_{v0}^+), Reynolds shear stress (τ_{R0}^+), and total shear stress (τ_{t0}^+) over the smooth and the SHS. The shear stresses are normalized by the wall shear stress of the smooth surface (τ_{w0}).

3.4 The shear-free pattern

For a SHS with an organized pattern of cavities or grooves, the morphology of the shear-free pattern can be inferred based on the surface pattern. However, this is more complex for a random surface due to the large spectrum of roughness elements and sensitivity of the plastron morphology to environmental parameters such as pressure and dissolved air. The recent visualization of Reholon & Ghaemi (2018) showed the presence of a full plastron for high DR ($> 16\%$) and isolated menisci of air, pinned between the tips and valleys of the roughness elements for lower DR ($< 8\%$) over a SHS with a random texture. To investigate the shear-free pattern of the SHS, the streamwise velocity measured in the immediate vicinity of the wall is used here.

The spatial distribution of temporally averaged velocity $\langle U^+ \rangle_t$ in an x - z plane with dimensions of $1000\lambda \times 1000\lambda$ ($13 \times 13 \text{ mm}^2$) at $y^+ = 3$ over the smooth and SHS are shown in figure 14. The velocity data corresponds to $2.5 < y^+ < 3.5$, binned into a grid of $75\lambda \times 75\lambda$ ($1 \times 1 \text{ mm}^2$) windows in the x - z plane. The $\langle U^+ \rangle_t$ distribution over the smooth surface in figure 14(a) shows a relatively uniform velocity distribution varying between $\langle U^+ \rangle_t \approx 2$ to 4. The variation is due to statistical convergence of the data when divided into the $1 \times 1 \text{ mm}^2$ windows. The $\langle U^+ \rangle_t$ contours over three separately fabricated SHSs are displayed in figure 14(b-d). The contours show higher streamwise velocity up to $\langle U^+ \rangle_t \approx 6$ in patches as large as $800\lambda \times 300\lambda$ ($13.6 \times 5.1 \text{ mm}^2$) in the x and z directions, respectively. The high-speed patches indicate regions of substantial streamwise slip due to a thicker underneath the layer of air.

The DNS of Seo & Mani (2018) showed that randomly distributed posts with similar height can interrupt the shear-free regions. This interruption resulted in smaller shear-free areas, which in turn generated a smaller effective slip length compared with an organized counterpart with streamwise-aligned posts. In the current investigation, the variation of protrusion height allows the shear-free regions to extend between the peaks of the larger protrusions without interruption by the smaller roughness elements. The SEM images and the profilometer measurements in §2.2 showed that the SHS roughness features with $\sim 20 \mu\text{m}$ height occur at a mean distance of about 12 mm, similar to the streamwise length of the shear-free regions (see figure 14(a)). This shows that the smaller peaks ($R < 20 \mu\text{m}$) do not disrupt the shear-free regions; the trapped air bubbles form a larger plastron pinned between the highest peaks. This is consistent with the DNS of Alame & Mahesh (2018) over a more realistic SHS with a random texture based on a 3D scan of a SHS. They numerically showed that a thicker air layer can generate larger shear-free regions since small roughness elements are covered with the air plastron.

3.5 Drag estimation

In this section, the DR is estimated using several techniques including pressure drop measurements, estimation of wall-shear stress, the logarithmic law, and the formulation of Rastegari & Akhavan (2015). The results are used to evaluate the analytical estimation of DR by Fukagata *et al.* (2006), which explicitly includes the streamwise and spanwise slip lengths (l_x and l_z).

Drag reduction from pressure drop measurement is expressed as $(dp_0 - dp)/dp_0$, where dp_0 is pressure drop along the smooth surface and dp is pressure drop along the SHS. Although this method is straightforward, it is subject to relatively large uncertainties due to the small pressure drop ($\sim 700 \text{ Pa}$) along the streamwise length of the SHS (240 mm) and partial coverage of the inner surface of the channel by the SHS coating. As previously discussed, the SHS is installed only at the top wall of the channel; however, the measured pressure drop is due to skin-friction on the whole interior of the channel. Therefore the drag reduction by the SHS is estimated as $\text{DR} = 2 \times (dp_0 - dp)/dp_0 = 30\%$, where following Gose *et al.* (2018) a factor of $2 \times$ is applied due

to partial coverage of the channel interior. Based on the error propagation theory (Hughes & Hase 2010) and the 2% uncertainty in pressure drop measurement, the uncertainty of the estimated DR is $\pm 8\%$. To check the repeatability of DR, pressure drop measurements were performed over two additional SHSs, showing 34 and 30% DR.

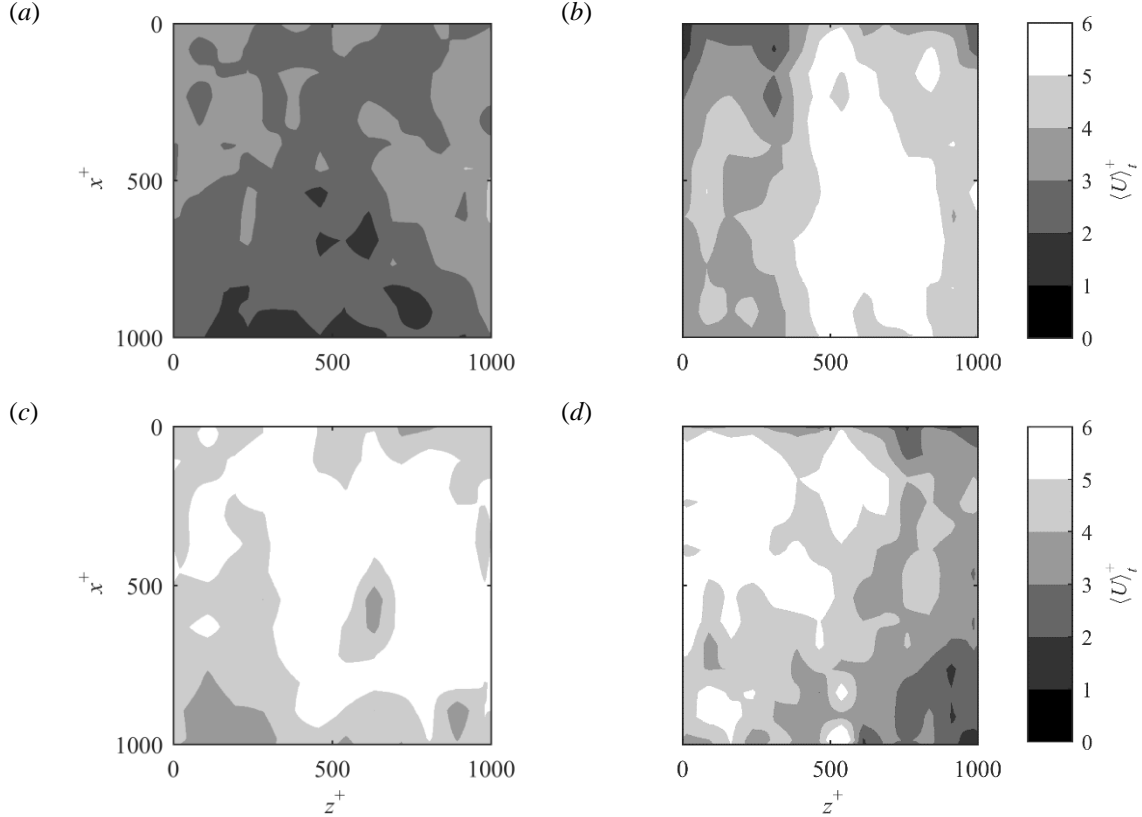


FIGURE 14. Mean velocity distribution over an x - z plane for (a) smooth and (b, c, and d) three sample SHSs. The velocity is averaged within $2.5 < y^+ < 3.5$ and a grid with $75\lambda_0 \times 75\lambda_0$ windows is considered to generate the contours.

Ling *et al.* (2016) estimated the DR over a SHS from direct measurement of wall shear stress (τ_w) as a summation of viscous stress ($\tau_w^\mu = \mu \partial \langle U \rangle / \partial y$) and Reynolds shear stress ($\tau_w^R = -\rho \langle uv \rangle$), where μ is the dynamic viscosity. As seen in figure 12(g), the Reynolds shear stress is expected to be negligible at $y^+ = 0$ over the current SHS due to its small roughness. Therefore the DR is estimated here as $(\tau_{w,0}^\mu - \tau_w^\mu) / \tau_{w,0}^\mu$, where the subscript 0 refers to wall shear stress over the smooth surface. The calculated DR is 38% based on wall shear stress estimated from the linear velocity gradient at $2.5 < y^+ < 3.5$.

The third method for estimating DR is based on a modification of the logarithmic law of the mean velocity profile as investigated by Min & Kim (2004), Fukagata *et al.* (2006), Busse & Sandham (2012), and Rastegari & Akhavan (2019). For a SHS with DR, the von Kármán constant, κ , remains unchanged while the intercept of the logarithmic profile B , increases as seen in figure 8(a). Following the formulation of Bechert *et al.* (1997) in a study of riblet surfaces, DR can be obtained from

$$\text{DR} = \frac{-\Delta B}{(2c_{f0})^{-1/2} + (2\kappa)^{-1}} \quad (3.1)$$

where ΔB is the change of the intercept of the logarithmic profile between the smooth and SHS, and the skin-friction coefficient is defined as $c_f = \tau_w / (\frac{1}{2}\rho U_b^2)$. The estimated DR from (3.1) is 36%. This method overestimates the DR by 4.0% compared with the DR obtained from the reduction of the wall shear stress. The high DR from (3.1) can be associated with the negligible effect of the spanwise slip on the mean streamwise velocity profile away from the wall due to its small magnitude as shown by Min & Kim (2004). In equation (3.1), ΔB is a function of surface structure while c_f depends on Re (Rastegari & Akhavan 2019).

Rastegari & Akhavan (2015) developed an expression to estimate DR over a wall with a slip-free boundary by decomposing the drag into a term due to slip velocity and another term due to modifications of the Reynolds shear stress based on the original formulation of Fukagata *et al.* (2002). This decomposition of DR is given by

$$\text{DR} = \frac{U_s}{U_b} + \left(1 - \frac{u_s}{U_b}\right) \left(\frac{3\varepsilon}{1 - 3I^+}\right). \quad (3.2)$$

Here $\varepsilon = I_0^+ - I^+$ is the difference between the weighted integrals of $\langle uv \rangle^+$ over the smooth and SHS, obtained from

$$I^+ = \int_0^1 (1 - \delta) \langle uv \rangle^+ d\delta, \quad (3.3)$$

where $\delta = 2y/H$ is the normalized wall-normal coordinate. The integrals over the two surfaces in (3.3) were carried out within $2.5 < y^+ < 90$ ($0.01 < \delta < 0.4$). The limited range of integration does not affect the estimated DR due to the negligible value of $(1-\delta)\langle uv \rangle^+$ at $y^+ < 2.5$ and farther away from the wall at $y^+ > 90$. The estimated DR from (3.2) is 35%.

The expression of DR from the theoretical study of Fukagata *et al.* (2006) includes both slip lengths (l_x and l_z) following

$$\kappa F_0 + \ln Re_{\tau 0} = (1 - \text{DR})\kappa l_{x0}^+ + \sqrt{1 - \text{DR}} \ln(\sqrt{1 - \text{DR}} Re_{\tau 0}) + \sqrt{1 - \text{DR}} \kappa F. \quad (3.4)$$

Here F_0 is obtained from $U_b/u_\tau = (\kappa^{-1} \ln Re_{\tau 0} + F_0)$ as expressed by Dean (1978) and is equal to 2.9. The parameter F is a function of the non-dimensionalized spanwise slip length (l_z^+). Fukagata *et al.* (2006) estimated F based on an exponential fit obtained from the numerical results of Min & Kim (2004) as

$$F = 4 \exp -(0.14 l_z^+)^{0.7} - 0.8. \quad (3.5)$$

This function results in $F \approx 0.75$ using the spanwise slip length obtained in subsection (3.2). The numerical solution of (3.4) results in a DR of 32%, which underestimates DR by 3-6% compared with the other techniques as shown in table 2. The low DR from (3.4) is associated with the estimated F from the DNS of Min & Kim (2004), which assumes a flat boundary condition. The analysis shows that spanwise slip should be measured over a wider range of conditions including Re_τ and k^+ to develop more accurate analytical models for the estimation of drag over SHS.

4. Summary and conclusion

The flow over a superhydrophobic surface (SHS) and a smooth baseline surface were characterized using a three-dimensional Lagrangian particle tracking velocimetry (3D-PTV) based on the shake-the-box method. A randomly textured SHS was generated using spray coating with a root-mean-square roughness of $4.9\mu\text{m}$ (0.29λ), and an average peak distance of $85\mu\text{m}$ (5.0λ). The inner scaling of flow over the SHS was $17\mu\text{m}$ and is indicated by λ . The surfaces were installed in a turbulent channel flow at constant mass flow rate with a Reynolds number of 7000 based on the bulk velocity and the full channel height. The friction Reynolds numbers over the smooth surface and SHS were 217 and 180, respectively.

Equation for estimation of DR	DR%
$\text{DR} = 2 \times \frac{dp_0 - dp}{dp_0}$	30 ± 8
$\text{DR} = \frac{\tau_{w_0} - \tau_w}{\tau_{w_0}}$	38
$\text{DR} = \frac{\Delta B}{(2c_{f_0})^{-1/2} + (2\kappa)^{-1}}$	36
$\text{DR} = \frac{u_s}{U_b} + \left(1 - \frac{u_s}{U_b}\right) \left(\frac{3\varepsilon}{1 - 3l^+}\right)$	35
$\kappa F_0 + \ln Re_{\tau_0} = (1 - \text{DR})\kappa l_{x_0}^+ + \sqrt{1 - \text{DR}} \ln(\sqrt{1 - \text{DR}} Re_{\tau_0}) + \sqrt{1 - \text{DR}} \kappa F$	32

TABLE 2. Summary of the estimated DR from pressure drop measurement, wall-shear stress, logarithmic law, the formulation of Rastegari & Akhavan (2015), and the analytical expression of Fukagata *et al.* (2006).

The 3D-PTV measurement of the mean velocity profiles over the SHS showed an increase of the mean streamwise velocity in the near-wall region, confirming the presence of a streamwise slip velocity. The extrapolation of the linear viscous sublayer to the wall indicated a slip velocity of 0.27 m/s (30% of the bulk velocity), which is associated with a streamwise slip length of $96.5\mu\text{m}$ (5.9λ). The scatter plot of spanwise particle velocity showed a large number of tracers with finite spanwise velocity at the SHS. The spanwise slip velocity was estimated to be 0.018 m/s from averaging the absolute values of spanwise velocity of the tracers. This is equivalent to a $95.8\mu\text{m}$ (5.9λ) spanwise slip length, which indicates a SHS with an isotropic slip with a similar slip length in the streamwise and spanwise directions. Farther away from the SHS, the effect of the slip velocity diminished and a smaller streamwise and spanwise velocity was observed compared with the smooth surface.

When dimensional Reynolds stresses over the smooth and SHS were compared at the same flow rate the streamwise and spanwise Reynolds stresses were larger in the near-wall region of the SHS. This indicates the presence of both streamwise and spanwise slip. The peaks of the streamwise and spanwise Reynolds stresses, when normalized by the smooth and the corresponding inner scaling, were also shifted closer to the wall due to the thinner inner layer over the SHS. The wall-normal Reynolds stress over the SHS remained comparable to the smooth surface in the near-wall region due to the non-permeable boundary condition of both surfaces. In the immediate vicinity of the wall, Reynolds shear stress over the SHS was slightly larger than that of the smooth surface. All components of the Reynolds stress tensor were smaller over the SHS farther away from the surface. However, when the Reynolds stresses were non-dimensionalized using the corresponding inner scaling of each surface they had a larger value

with respect to the smooth surface across the inner layer. This indicates that normalization of Reynolds stresses using inner scaling does not result in overlap of Reynolds stress profiles when slip velocity is present.

The patterns of the shear-free regions were also investigated over the SHS using contours of near-wall mean streamwise velocity in a streamwise/spanwise plane at $y^+=3$. The results showed streamwise-elongated patches of high streamwise velocity over the SHS, which represent the morphology of the underneath air layer. The high-speed regions were up to $800\lambda \times 300\lambda$ (13.6×5.1 mm²) in the streamwise and spanwise directions, respectively. The SEM images and the profilometer measurements also showed that the largest roughness features with ~ 20 μm height occur at a mean distance of about 12 mm similar to the streamwise length of the largest shear-free regions. Therefore the smaller roughness peaks do not disrupt the shear-free regions as the plastron is pinned between the highest peaks. The drag reduction (DR) over the current SHS was estimated and evaluated using various techniques. The results indicated DR of about 30 to 38% over the investigated SHS.

Acknowledgements

This work was supported under the Natural Sciences and Engineering Research Council of Canada (NSERC RGPIN 1512 GHAEMI).

Appendix

Uncertainty evaluation

The measurement noise of the 3D-PTV system is evaluated here using statistical convergence of the turbulence parameters. Figure 15 shows statistical convergence of U^+ , W^+ , and the four components of $\langle u_i u_j \rangle^+$ at $y^+ = 40$ over the smooth surface. The U^+ , W^+ , and $\langle u_i u_j \rangle^+$ data are averaged over bins with 10, 30, and 50 μm length in the wall-normal direction, respectively, similarly to the averaging of section 3. The horizontal axis of figure 15 shows the number of data points (n) normalized with the total number of data points (N). It is seen in figure 15(a) that U^+ quickly reaches statistical convergence. The difference of the minimum and maximum values (peak-to-peak) of average U^+ in the last 20% of the data ($n/N = 0.8$ to 1) is 0.06%. Figure 15(b) shows a larger range of noise of 0.40% based on peak-to-peak value for W^+ . Figures 15(c) and 15(d) show that $\langle u^2 \rangle^+$ and $\langle v^2 \rangle^+$ converge at $n/N = 0.8$ with 0.40 and 0.30% random noise, respectively. The largest peak-to-peak noise is observed for $\langle w^2 \rangle^+$ and is 0.50% as seen in figure 15(e). The average $\langle uv \rangle^+$ in figure 15(f) converges faster than $\langle u^2 \rangle_0^+$ and $\langle v^2 \rangle_0^+$, with 0.46% peak-to-peak noise between $n/N = 0.8$ to 1. The evaluation of the random noise for the 3D-PTV measurement of the mean velocities and Reynolds stresses over the smooth surface is summarized in table 3. The percentages of peak-to-peak variation based on statistical convergence at the three wall locations of $y^+ = 15, 30,$ and 45 are presented in table 3. The noise level reduces by moving away from the wall where the displacement of the particles is larger, and the fluctuations are smaller.

The number of data points versus the wall-normal location for 10, 30, and 50 μm bins (75% overlap) is shown in figure 16. The 10, 30, and 50 μm bins are used to obtain $\langle U \rangle$, $\langle |W| \rangle$, and $\langle u_i u_j \rangle$, respectively. The average number of data along y^+ for the 10, 30, and 50 μm bins is 1.7×10^4 , 5.4×10^4 , and 9.3×10^4 , respectively.

Parameter	$y^+ = 15$	$y^+ = 30$	$y^+ = 45$
$\langle U \rangle^+$	0.60%	0.11%	0.06%
$\langle W \rangle^+$	0.51%	0.31%	0.24%
$\langle u^2 \rangle_0^+$	0.77%	0.60%	0.28%
$\langle v^2 \rangle_0^+$	0.90%	0.54%	0.30%
$\langle w^2 \rangle_0^+$	0.91%	0.52%	0.48%
$\langle uv \rangle_0^+$	0.82%	0.68%	0.44%

TABLE 3. Random noise of the mean velocities and Reynolds stresses over the smooth surface at $y^+ = 15, 30$ and 45.

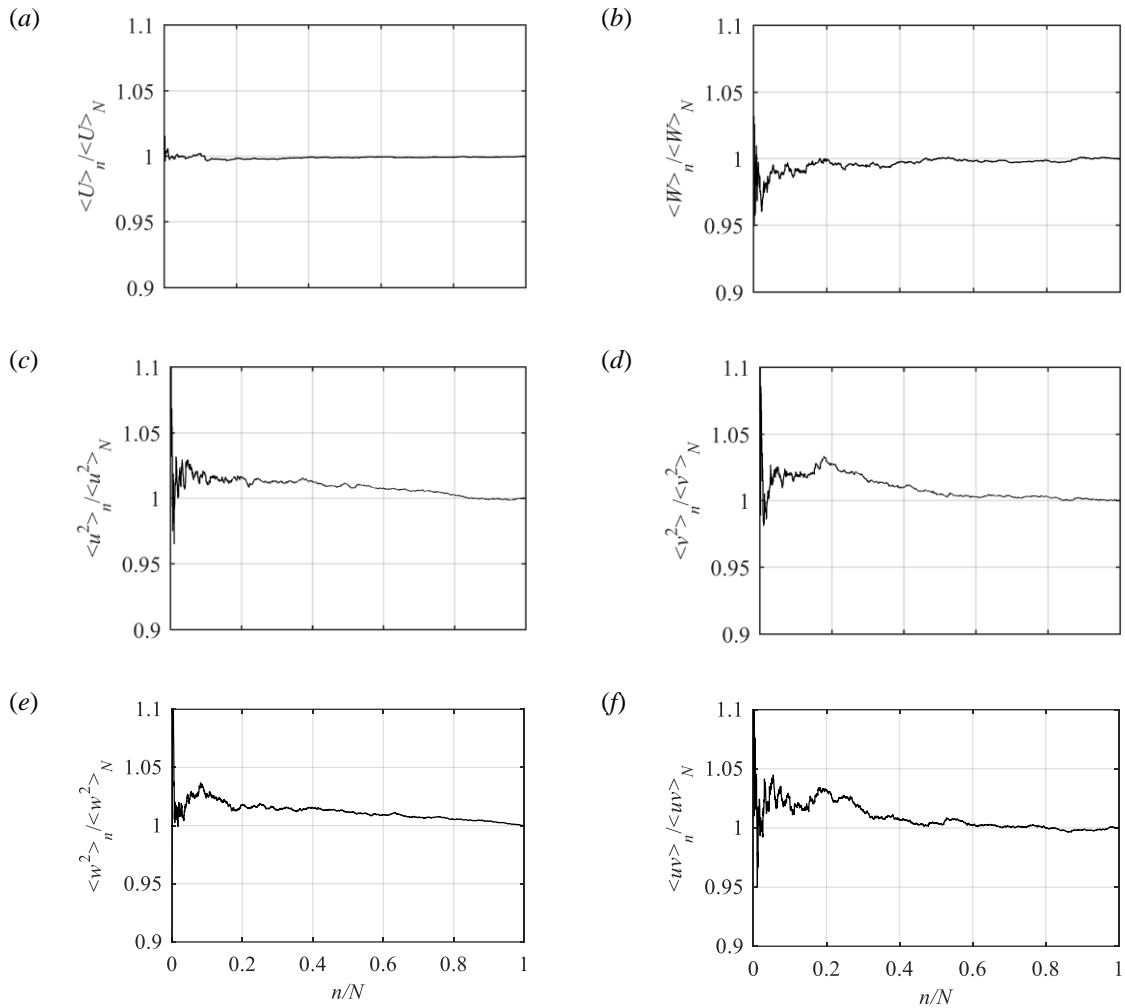


FIGURE 15. Statistical convergence of (a) U_0^+ , (b) W_0^+ , (c) $\langle u^2 \rangle_0^+$, (d) $\langle v^2 \rangle_0^+$, (e) $\langle w^2 \rangle_0^+$, and (f) $\langle uv \rangle_0^+$ over the smooth surface at $y^+ = 40$. Each component of the mean velocities and Reynolds stress tensors are normalized by their own mean tensor at $y^+ = 40$.

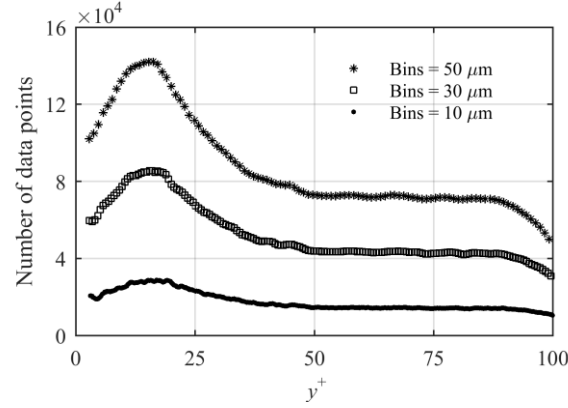


FIGURE 16. Number of data points for three different bin sizes along the y axis.

Effect of temporal regression on particle position spectra

The performance of the second-order temporal filter of Section 2.3 is evaluated here by plotting the pre-multiplied linear spectral density (LSD) of the x , y , and z components of the particle trajectories (Gesemann *et al.* (2016)). The pre-multiplied LSD for the trajectories with and without the temporal filter is plotted as a function of frequency in figure 17. Frequency (f) is normalized using the Nyquist frequency (f_N). The LSD profiles with and without the regression filter overlap at low frequencies until a cross-over frequency. Beyond this cross-over frequency, the LSD of trajectories without the temporal filter becomes flat (white noise). The estimated cross-over frequency is at about 1100, 1200, and 300 Hz for the x , z , and y components. This results in an estimated noise wavelength of 3.6, 11.4 and 3.3 time steps (Δt) based on the acquisition frequency of 4000 Hz. The flat region also corresponds to pre-multiplied LSD values of 3.5, 3.2, and 7 μm , which are equivalent to 0.1, 0.1, 0.2 pix in the x , z , and y -directions, respectively. This estimated uncertainty of particle position agrees with the expected accuracy for the in-plane and out-of-plane components of particle tracking methods before applying a temporal filter. The temporal filter has a negligible effect on the low-frequency content while it significantly reduces the random noise of higher frequencies as seen in figure 17.

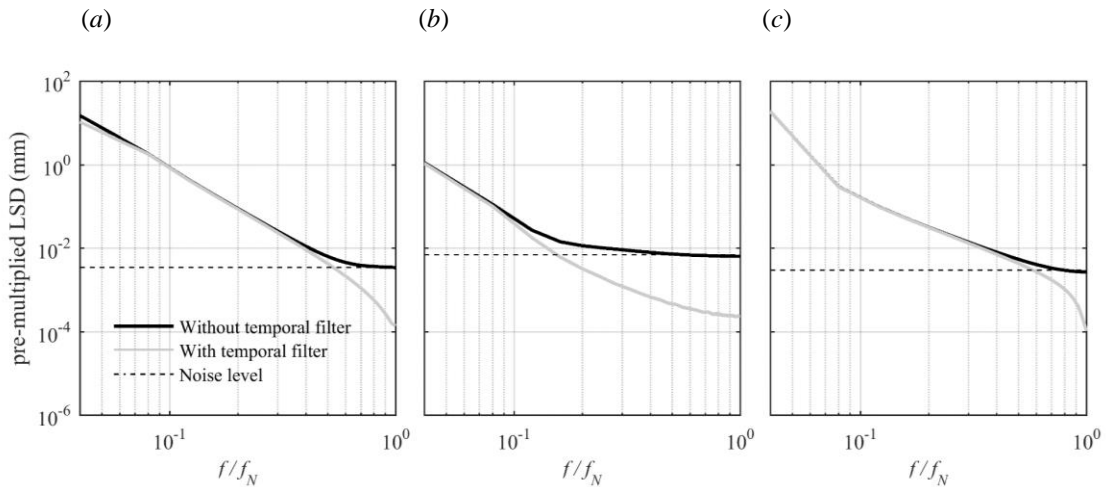


FIGURE 17. Pre-multiplied LSD of the (a) x , (b) y , and (c) z components of particle position with and without the temporal filter.

References

- ABU ROWIN, W., HOU, J. & GHAEMI, S. 2017 Inner and outer layer turbulence over a superhydrophobic surface with low roughness level at low Reynolds number. *Phys. Fluids* **29** (9), 095106.
- ABU ROWIN, W., HOU, J. & GHAEMI, S. 2018 Turbulent channel flow over riblets with superhydrophobic coating. *Exp. Therm. Fluid. Science* **94**, 192–204.
- ALAM K. & MAHESH, K. Wall-bounded flow over a realistically rough superhydrophobic surface. *J. Fluid Mech.*, in press.
- ALJALLIS, E., SARSHAR, M. A., DATLA, R., SIKKA, V. & JON A. 2013 Experimental study of skin friction drag reduction on superhydrophobic flat plates in high Reynolds number boundary layer flow. *Phys. Fluids* **25**, 025103.
- BECHERT, D., BRUS M., HAG W., van der HOEVEN, J. & HOPP G. 1997 Experiments on drag-reducing surfaces and their optimization with an adjustable geometry. *J. Fluid Mech.* **338**, 59–87.
- BUSS A. & SANDHAM, N. D. 2012 Influence of an anisotropic slip-length boundary condition on turbulent channel flow. *Phys. Fluids* **24**, 055111.
- CHOI, C. H., ULMANELLA, U., KIM, J., HO, C. M. & KIM, C. J. 2006 Effective slip and friction reduction in nanogated superhydrophobic microchannels. *Phys. Fluids* **18**, 087105.
- CLAUSER, F. H. 1956 The turbulent boundary layer. In *Advances in applied mechanics* **4**, 1–51.
- DANIELLO, R., WATERHOUS N. E. & ROTHSTEIN, J. P. 2009 Turbulent drag reduction using superhydrophobic surfaces. *Phys. Fluids* **21**, 085103.
- DEAN, R. B. 1978 Reynolds number dependence of skin friction and other bulk flow variables in two-dimensional rectangular duct flow. *Trans. ASME J. Fluids Eng.* **100** (2), 215–223.
- DILIP, D., JHA, N.K., GOVARDHAN, R.N. & BOBJI, M.S., 2014 Controlling air solubility to maintain “Cassie” state for sustained drag reduction. *Colloids and Surfaces A: Physicochemical and Engineering Aspects* **459**, 217–224.
- FUKAGATA, K., IWAMOTO, K. & KASAGI, N. 2002 Contribution of Reynolds stress distribution to the skin-friction in wall-bounded flows. *Phys. Fluids* **14**, L73–L76.
- FUKAGATA, K., KASAGI, N. & KOUMOUTSAKOS, P. 2006 A theoretical prediction of friction drag reduction in turbulent flow by superhydrophobic surfaces. *Phys. Fluids* **18**, 051703.
- GESEMANN, S., HUHN, F., SCHANZ, D. & SCHRÖDER, A., 2016. From noisy particle tracks to velocity, acceleration and pressure fields using B-splines and penalties, 18th International Symposium on the Applications of Laser and Imaging Techniques to Fluid Mechanics (Lisbon, Portugal, 4–7 July)
- GILBERT, N. & KLEISER, L. 1991 Turbulence model testing with the aid of direct numerical simulation results. *Proc. 8th Symposium on Turbulent Shear Flows*, Sept. 9-1 I, Munich, Germany.
- GOS J. W., GOLOVIN, K., BOBAN, M., MABRY, J. M., TUTEJA, A., PERLIN, M. & CECCIO, S. L. 2018 Characterization of superhydrophobic surfaces for drag reduction in turbulent flow. *J. Fluid Mech.* **845**, 560–580.
- HUGHES, I. & HAS T. 2010. *Measurements and their uncertainties: a practical guide to modern error analysis*. Oxford University Press. 37-51

- JOSEPH, P., COTTIN-BIZONN C., BENOT, J.-M., YBERT, C., JOURNET, C., TABELING, P. & BOCQUET, L. 2006 Slippage of water past superhydrophobic carbon nanotube forests in microchannels. *Phys. Rev. Lett.* **97** (15), 156104.
- KÄHLER, C.J., SCHARNOWSKI, S. & CIERPKA, C. 2012 On the uncertainty of digital PIV and PTV near walls. *Exp. Fluids* **52**(6), 1641–1656.
- KIM, J., MOIN, P. & MOSER, R. 1987 Turbulence statistics in fully developed channel flow at low Reynolds number. *J. Fluid Mech.*, **177**, 133–166.
- LEE J., JELLY, T. O. & ZAKI, T. A. 2015 Effect of Reynolds number on turbulent drag reduction by superhydrophobic surface textures. *Flow Turbul. Combust.* **95**, 277–300.
- LEI, L., LI, H., SHI, J. & CHEN, Y. 2009 Diffraction patterns of a water-submerged superhydrophobic grating under pressure. *Langmuir*. **26**(5), 3666–3669.
- LING, H. 2017. Experimental Investigation of Friction Drag Reduction in Turbulent Boundary Layer by Super-Hydrophobic Surfaces (Doctoral dissertation, Johns Hopkins University).
- LING, H., KATZ, J., FU, M. & HULTMARK, M. 2017 High-resolution velocity measurement in the inner part of turbulent boundary layers over super-hydrophobic surfaces. *J. Fluid Mech.* **801**, 670–703.
- LING, H., SRINIVASAN, S., GOLOVIN, K., MCKINLEY, G.H., TUTEJA, A. & KATZ, J. 2016 Effect of Reynolds number and saturation level on gas diffusion in and out of a superhydrophobic surface. *Phys. Rev. Fluids*. **801**, 670–703.
- MARTELL, M. B., PEROT, J. B. & ROTHSTEIN, J. P. 2009 Direct numerical simulations of turbulent flows over superhydrophobic surfaces. *J. Fluid Mech.* **620**, 31–41.
- MARTELL, M. B., ROTHSTEIN, J. P. & PEROT, J. B. 2010 An analysis of superhydrophobic turbulent drag reduction mechanisms using direct numerical simulation. *Phys. Fluids* **22**, 065102.
- MIN, T. & KIM, J. 2004 Effects of hydrophobic surface on skin-friction drag. *Phys. Fluids* **16**, L55–L58.
- NOVARA, M., SCHANZ, D., REUTHER, N., KÄHLER, C.J. & SCHRÖDER, A. 2016 Lagrangian 3D particle tracking in high-speed flows: Shake-The-Box for multi-pulse systems. *Exp. Fluids*, **57**(8), 128.
- Ou, J., Perot, J. B. & Rothstein, J. 2004 Laminar drag reduction in microchannels using superhydrophobic surfaces. *Phys. Fluids* **16** (12), 4635–4643.
- Ou, J. & Rothstein, J. 2005 Direct velocity measurements of the flow past drag-reducing ultrahydrophobic surfaces. *Phys. Fluids* **17** (10), 13606:2–13606:10.
- PARK, H., PARK, H. & KIM, J. 2013 A numerical study of the effects of superhydrophobic surface on skin-friction drag in turbulent channel flow. *Phys. Fluids* **25**, 110815.
- PARK, H., SUN, G. & KIM, C.-J. 2014 Superhydrophobic turbulent drag reduction as a function of surface grating parameters. *J. Fluid Mech.* **747**, 722–734.
- RASTEGARI, A. & AKHAVAN, R. 2015 On the mechanism of turbulent drag reduction with superhydrophobic surfaces. *J. Fluid Mech.* **773**, R4.
- RASTEGARI, A. & AKHAVAN, R. 2019 On drag reduction scaling and sustainability bounds of superhydrophobic surfaces in high Reynolds number turbulent flows. *J. Fluid Mech.* **864**, 327–347.
- REHOLON, D & GHAEMI, S., 2018. Plastron morphology and drag of a superhydrophobic surface in turbulent regime. *Phys. Rev. Fluids*, 3(10), 104003.
- ROTHSTEIN, J. P. 2010 Slip on superhydrophobic surfaces. *Annu. Rev. Fluid Mech.* **42**, 89–109.

- SAMAHA, M. A., TAFRESHI, H. V. & GAD-EL-HAK, M. 2012a Influence of flow on longevity of superhydrophobic coatings. *Langmuir* **28**, 9759–9766.
- SCARANO, F. 2012 Tomographic PIV: principles and practice. *Measurement Science and Technology* **24**(1), 012001.
- SCHANZ, D., GESEMANN, S., SCHRÖDER, A., WIENEK B. & NOVARA, M. 2012. Non-uniform optical transfer functions in particle imaging: calibration and application to tomographic reconstruction. *Measurement Science and Technology* **24**(2), 024009.
- SCHANZ, D., SCHRÖDER, A., GESEMANN, S. & WIENEK B. 2013 ‘Shake The Box’: A highly efficient and accurate Tomographic Particle Tracking Velocimetry (TOMO-PTV) method using prediction of particle positions. 10th International Symposium on Particle Image Velocimetry. Delft, the Netherlands.
- SCHANZ, D., GESEMANN, S. & SCHRÖDER, A. 2016 Shake-The-Box: Lagrangian particle tracking at high particle image densities. *Exp. Fluids* **57**(5), 70.
- SCHRÖDER, A., SCHANZ, D., Geisler, R., GESEMANN, S. & WILLERT, C. 2015 Near-wall turbulence characterization using 4D-PTV Shake-The-Box. In: 11th international symposium on particle image velocimetry-PIV15. Santa Barbara, California, 14–16 Sept 2015
- SEO, J., GARCÍA-MAYORAL, R. & MANI, A. 2018 Turbulent flows over superhydrophobic surfaces: flow-induced capillary waves, and robustness of air–water interfaces. *J. Fluid Mech.* **835**, 45–85.
- SEO, J. & MANI, A. 2018 Effect of texture randomization on the slip and interfacial robustness in turbulent flows over superhydrophobic surfaces. *Phys. Rev. Fluids*. **3**(4), 044601.
- TÜRK, S., DASCHIEL, G., STROH, A., HASEGAWA, Y. & FROHNAPFEL, B. 2014 Turbulent flow over superhydrophobic surfaces with streamwise grooves. *J. Fluid Mech.* **747**, 186–217.
- VAJDI HOKMABAD, B. & GHAEMI, S. 2016 Turbulent flow over wetted and non-wetted superhydrophobic counterparts with random structure. *Phys. Fluids* **28** (1), 015112.
- VAJDI HOKMABAD, B. & GHAEMI, S. 2017 Effect of flow and particle-plastron collision on the longevity of superhydrophobicity. *Scientific Reports*. **7**, 41448.
- VINUESA, R., NOORANI, A., LOZANO-DURÁN, A., KHOURY, G.K.E., SCHLATTER, P., FISCHER, P.F. & NAGIB, H.M. 2014. Aspect ratio effects in turbulent duct flows studied through direct numerical simulation. *Journal of Turbulence*, **15**(10), 677-706.
- VOTH, G. A., LA PORTA, A., CRAWFORD, A. M., ALEXANDER, J. & BODENSCHATZ, E. 2002 Measurement of particle accelerations in fully developed turbulence. *J. Fluid Mech.* **469**, 121–160.
- WIENEK B. 2008 Volume self-calibration for 3D particle image velocimetry. *Exp. Fluids* **45**(4), 549–556.
- WIENEK B. 2012 Iterative reconstruction of volumetric particle distribution. *Measurement Science and Technology*, **24**(2), 024008.
- WOOLFORD, B., PRINC J., MAYNES, D. & WEBB, B. W. 2009 Particle image velocimetry characterization of turbulent channel flow with rib patterned superhydrophobic walls. *Phys. Fluids* **21**, 085106.
- YOUNG, T. 1805 An essay on the cohesion of fluids. *Phil. Trans. R. Soc. Lond.* **95**, 65–87.
- ZHANG, J., TIAN, H., YAO, Z., HAO, P. & JIANG, N. 2015 Mechanisms of drag reduction of superhydrophobic surfaces in a turbulent boundary layer flow. *Exp. Fluids* **56**, 179.